eman ta zabal zazu
Universidad del País Vasco
Euskal Herriko Unibertsitatea
ZIENTZIA ETA TEKNOLOGIA FAKULTATEA
FACULTAD DE CIENCIA Y TECNOLOGÍA

Bachelor's Thesis
Degree in Physics

Active photonic devices based on spintronic-plasmonic metasurfaces

Author:
Ángela Díez Sánchez

Supervisor:
Miren Nerea Zabala Unzalu

Leioa, June 2023

Acknowledgements

First of all, I would like to express my deep gratitude to my supervisor, Dr. Nerea Zabala, for her invaluable advice and continue support, guidance and encouragement throughout the elaboration of this thesis. I would also like to thank Dr. Luca Bergamini and Dr. Jose Luis Montaño Priede for their additional help on my study. Lastly, I would like to thank my parents and close friends for coming along with me in this whole journey.

Abstract

In this work, we study the magnetic field modulation of the optical response of plasmonic-spintronic metasurfaces. The responsible effect of this modulation is the Magneto-refractive effect (MRE), which accounts for the magnetic field induced modification of the electrical resistivity that translates into a change in the optical properties, making it possible to magnetically modulate the plasmon resonances from the mid-infrared to the THz regime. First, we introduce concepts relevant to this work, such as Giant Magnetoresistance (GMR) and Surface Plasmons, which are resonant collective oscillations of conduction electrons that can be localized in the surface of a metallic nanoparticle or can propagate along a dielectric-metallic interface. Then, we study the MRE exhibited by GMR systems, more specifically by a $Ni_{81}Fe_{19}$/Au GMR multilayer. Finally, we present an analysis of the optical response of plasmonic metasurfaces fabricated out of the previously mentioned GMR multilayers, using the *Lumerical* software for the photonic simulations. We consider periodical structures such as nanoantenna- and hole-arrays, in order to demonstrate that metasurfaces made out of GMR multilayers can be utilized to develop active photonic platforms whose optical response is controlled by an external magnetic field.

Resumen

En este trabajo, estudiamos la modulación a través del campo magnético de la respuesta óptica de metasuperficies plasmónicas-espintrónicas. El efecto responsable de esta modulación es el Efecto Magneto-Refractivo (MRE), que explica la modificación inducida por el campo magnético de la resistividad eléctrica, que lleva asociado un cambio en las propiedades ópticas, permitiendo así modular magnéticamente las resonancias plasmónicas desde la región del infrarrojo medio hasta el régimen de los terahercios. En primer lugar, introducimos conceptos fundamentales del trabajo, como la Magnetoresistencia Gigante (GMR) y los plasmones de superficie, que son oscilaciones colectivas resonantes de los electrones de conducción que pueden estar localizadas en la superficie de una nanopartícula metálica o se pueden propagar a lo largo de una interfaz diélectrico-metal. Posteriormente, estudiamos el MRE que presentan sistemas con GMR, específicamente por una multicapa de $Ni_{81}Fe_{19}$/Au con GMR. Por último, presentamos un análisis de la respuesta óptica de metasuperficies plasmónicas fabricadas a partir de las previamente mencionadas multicapas, usando el software *Lumerical* para las simulaciones fotónicas. Consideramos estructuras periódicas como redes de nanoantenas y agujeros, con el fin de demostrar que las metasuperficies hechas de multicapas de GMR pueden ser utilizadas para desarrollar plataformas fotónicas activas cuya respuesta óptica es controlada por un campo magnético externo.

Laburpena

Lan honetan, eremu magnetikoaren bidezko erantzun optikoaren modulazioa aztertu dugu metagainazal plasmoniko espintronikoetan. Modulazio honen eragilea Efektu Magneto-Errefraktiboa (MRE) da, eremu magnetikoak eragindako erresistentzia elektrikoaren aldaketa azaltzen duena eta honen ondoriozko propietate optikoen aldaketak azaltzen dituena. Erresonantzia plasmonikoen modulazio magnetikoa infragorri ertainetik THz erregimenara posible egiten du efektu honek. Lehenik eta behin, lan honetan funtsezkoak diren kontzeptuak aurkezten ditugu, hala nola Magneto Erresistentzia Erraldoia (GMR) eta gainazaleko plasmoiak. Gainazaleko plasmoiak eroankortasuneko elektroien talde-oszilazio erresonantziak dira, nanopartikula metalikoen gainazalean gerta daitezkeenak, edo dielektriko-metal gainazaleetan zehar heda daitezkeenak. Ondoren, GMR sistema berezietan, zehazki, GMR $Ni_{81}Fe_{19}$/Au multigeruzetan, adierazten den MREa aztertu dugu. Azkenik, lehen aipatutako multigeruzekin fabrikatutako metagainazal plasmonikoen erantzun optikoaren analisia egiten dugu, *Lumerical* softwarea erabiliz simulazio fotonikoak egiteko. Nanoantena- eta zulo-sareak bezalako estruktura periodikoak aztertzen ditugu, GMR multigeruzekin egindako metagainazalek plataforma fotoniko aktiboak garatzeko erabil daitezkeela, eta haien erantzun optikoa kanpoko eremu magnetikoaren bidez kontrolagarria dela erakusteko.

Contents

1. Introduction and objectives

Plasmons are resonant collective oscilations of the conduction electrons excited by electromagnetic fields, which have played a key role in the development of different types of optical sensing platforms. Plasmonic metasurfaces are nanostructured materials capable of manipulating light (electromagnetic waves) from the visible to the microwave spectral range using smartly designed, two-dimensional arrangements of subwavelength plasmonic building blocks (scatterers) [1],[2],[3]. The capability of these structures to interact with light is determined basically by the intrinsic optical properties of their constituent materials, their size, shape, and spatial distribution [4]. Plasmonic resonant nanostructures have the ability of localizing and enhancing electromagnetic fields, acting as optical nanoantenna.

In order to increase the versatility of metasurfaces, active components have been incorporated in their design, which are materials whose optical response can be changed by applying an external stimulus [5]. Recently, Giant Magnetoresistance (GMR) multilayers have been incorporated into the list of components for the fabrication of active metasurfaces [6], [7]. These multilayers are fabricated by alternating ferromagnetic and non-ferromagnetic layers of nanometrical thickness. The GMR, sketched in Figure 1(a), is the most representative effect of spintronics. It stems from the dependence of the resistivity of a system on the relative orientation of the electron spin and the local magnetization, so that the application of an external magnetic field decreases dramatically the resistivity.

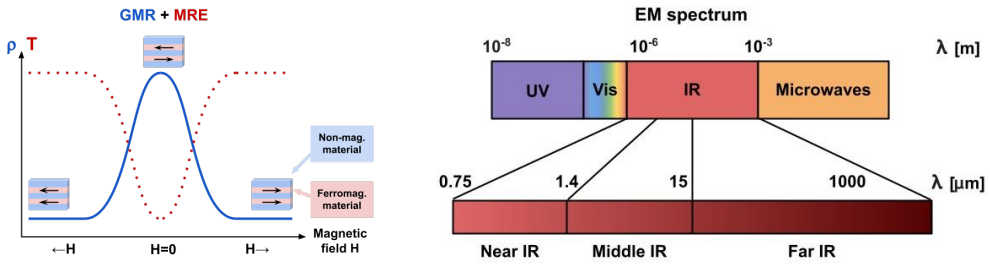

(a) (b)

Figure 1: (a) Schematic diagram of the magnetic-field **H** dependence of the resistivity ρ and optical transmittance T of a GMR multilayer composed of alternating layers of non-ferromagnetic and ferromagnetic metals. In the abscence of a magnetic field, the magnetizations of the adjacent ferromagnetic layers are antiparallel and the resistivity is much higher than in the presence of a magnetic field, when the magnetizations of the contiguous ferromagnetic layers are parallel. This change in the resistivity produces a change in the optical properties: Magneto-refractive effect (MRE). (b) The modulation of the optical response of spintronic-plasmonic metasurfaces may be extended into mid-far IR spectral range.

This new approach of using GMR multilayers as the active component of plasmonic metasurfaces combines both fields of spintronics and plasmonics, by exploiting the spin character of the conduction electrons via the spin-dependent electron transport properties. These spintronic–plasmonic metasurfaces have the peculiarity that their optical response can be modulated in the Mid and Far IR, fast and contactless, by applying a very low magnetic field. This is a consequence of the Magneto-refractive effect (MRE) [8], which accounts for the change in the optical constants of the GMR multilayer due to the modification of the electrical resistivity induced by the magnetic field, therefore

leading to a change of the diagonal elements of the dielectric tensor, which determines the optical response. In conclusion, active photonic devices based on spintronic nanostructures rely on the manipulation of the spin-dependent electronic and optical properties.

For the MRE effect to be efficiently transferred into an enhanced modulated-optical response, structures showing plasmonic resonances (plasmonic metasurfaces) appear as best-suited candidates [9]. Among some of the simplest examples of spintronic-plasmonic metasurfaces we found the GMR multilayer systems composed of metallic rods or slits. Some SEM (Scanning Electron Microscopy) images of these metasurfaces are shown in Figure 2.

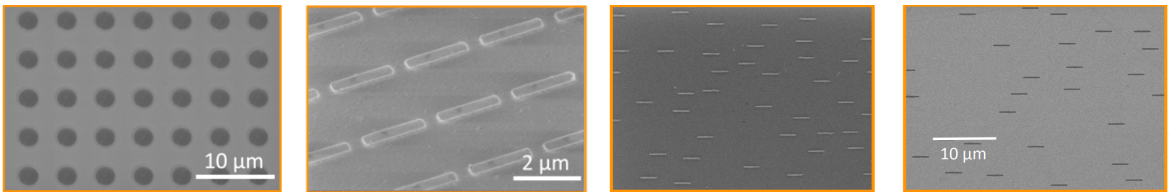

(a) (b) (c) (d)

Figure 2: SEM images of different metasurfaces of GMR multilayers, obtained from [5] and [9]: (a) Hole array, (b) Micro-antenna array, (c) Random rod array and (d) Random slit array.

This enhanced optical response of plasmonic-spintronic metasurfaces can be extremely useful for different applications. For instance, a plasmonic metasurface consisting of an array of metallic rod antennas fabricated out of a GMR multilayer, like the one shown in Figure 3(c), has been proposed to unambiguously identify molecules in the mid- and far-infrared [10]. Molecules are deposited on top of rough metallic surfaces with the intention of increasing the intensity of their specific vibration signal (Figure 3(c)) that allows us to directly detect them. This process is known as Surface-Enhanced Infrared Absorption (SEIRA) spectroscopy [11], [12]. This signal can be further increased by nanostructuring the metallic surface or by using arrays of metallic antennas, as the ones shown in Figure 2. In all these surfaces, plasmons are responsible for the electromagnetic field enhancement at the position of the molecule, which results in the increase of the vibration signal. The vibrational signals of most molecules are located in the mid-IR, as shown in Figure 3(a). Their signal is enhanced if the plasmon resonance matches the molecular vibration, as sketched in Figure 3(b).

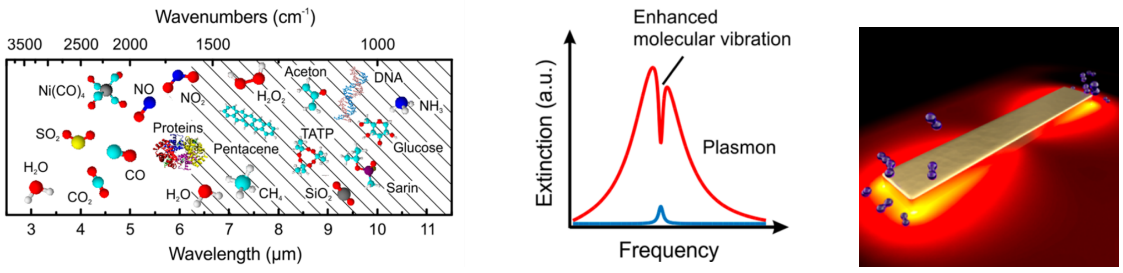

(a) (b) (c)

Figure 3: (a) Characteristic infrared vibrations of selected molecular species. (b,c) Principle of SEIRA: Infrared vibrations of molecules located in the enhanced electromagnetic near-field of a plasmonic nanostructure (nanoantenna) are enhanced if the plasmon (red) is resonantly matched to the molecular vibration (blue). All pictures obtained from [13].

The main objective of this work is to study how GMR multilayers can be utilized to develop an active photonic sensing platform, combining both plasmonics and spintronics, and to understand the principles behind both disciplines. Furthermore, the following specific objectives are set:

- To gain insight into Surface Plasmons (SPs).
- To understand the working principles of the Giant Magnetoresistance (GMR).
- To familiarise with the photonic simulation software *Lumerical*.
- To comprehend the Magneto-refractive effect (MRE) and its role in GMR systems.
- To analyse the obtained results and draw conclusions from them.
- To learn about research methodology.

Based on these objectives, the work has been structured as follows:

In section 2, **Surface Plasmons**, the theoretical concepts to have a better understanding of plasmonics and more precisely of the surface plasmons are introduced. Then, in section 3, **Spintronic-plasmonic metasurfaces**, the effect of the Giant Magnetoresistance is properly explained and followed by the description of the Magneto-refractive effect and its role in GMR multilayer systems. In section 4, **Simulations of the optical response**, the Finite-difference time-domain (FDTD) method used by the *Lumerical* software used to perform the simulations of the optical response is introduced, followed by the presentation of the discussed results. Finally, section 5 contains the main conclusions of this work.

2. Surface Plasmons (SPs)

Surface plasmons (SPs) are coherent collective electron oscillations propagating along a dielectric-metal interface [14], as sketched in Figure 4(a). They are classified as either Surface Plasmon Polaritons (SPPs), Figure 4(a), or Localized Surface Plasmons (LSPs), Figure 4(b). The latter are the result of the confinement of surface plasmon oscillations in a nanoparticle, and can be considered as the stationary waves of the eletron cloud oscillations when a small spherical metallic nanoparticle is irradiated by light. On the other hand, Surface Plasmon Polaritons (SPPs) are electromagnetic waves that exist at the interface between a metal and a dielectric material, such as air or water. These electromagnetic surface waves arise via the coupling of the electromagnetic fields to oscillations of the conductor's electron plasma [15]. When light hits the metal-dielectric interface at a certain angle, it excites the free electrons in the metal, and causes them to move in a wave-like motion, creating an oscillation of the electric field that travels along the metal's surface. This wave is called a Surface Plasmon Polariton. In this work, and namely in this whole section, we have mainly studied SPPs.

SPPs play a key role in the field of plasmonics, which studies the optical properties of metals and other materials at the nanoscale. Since the excitation of SPPs allows to overcome the diffraction limit by confining and enhancing the electromagnetic fields in space regions smaller than the wavelength of exciting light, they offer a promising approach to control and manipulate the propagation and dispersion of light at the nanometre scale. Therefore, they are extremely useful for technologies like nanoscale optics and sensors, and have potential applications in areas such as data storage and energy conversion [16].

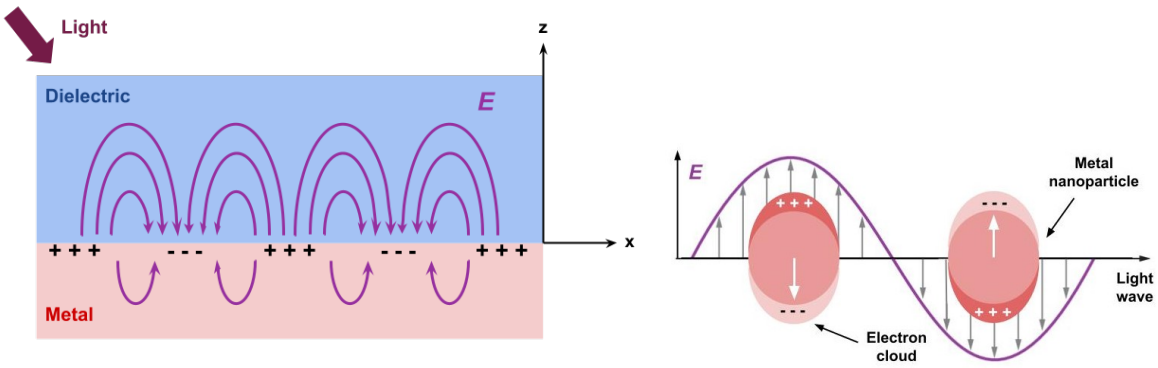

(a) (b)

Figure 4: (a) Schematic diagram of a SPP propagating across the interface between a conductor and a dielectric. (b) Schematic diagram of the oscillation of the conduction electrons of a metal nanoparticle, i.e. the localized surface plasmon (LSP).

In order to understand the interaction of light with metal structures, and therefore SPPs, we have to study the frequency dependence of the metal's complex dielectric function, so we begin with a discussion of the fundamental optical properties of metals.

2.1. Optical properties and dielectric function

The optical properties of metals can be described by a complex dielectric function that depends on the frequency of exciting light [17]. The macroscopic polarization $\mathbf{P}$, that appears as a result of the induced individual dipole moments of all free electrons, is given by the following equation, in which ε_0 is the permittivity of vacuum, χ_e the electric susceptibility and $\mathbf{E}$ the external electric field that oscillates with frequency ω.

$$\mathbf{P}(\omega) = \varepsilon_0 \ \chi_e(\omega) \ \mathbf{E}(\omega). \tag{1}$$

The electric displacement $\mathbf{D}$ is then written as:

$$\mathbf{D}(\omega) = \varepsilon_0 \ \varepsilon(\omega) \ \mathbf{E}(\omega) = \varepsilon_0 \ \mathbf{E}(\omega) + \mathbf{P}(\omega). \tag{2}$$

Combining both equations, we obtain the frequency-dependent dielectric function of the metal:

$$\varepsilon(\omega) = 1 + \chi_e(\omega). \tag{3}$$

The polarization $\mathbf{P}$ is easily obtained by solving the equation of motion of the electrons under the influence of an external field and knowing that $\mathbf{P} = n\mathbf{p} = ne\mathbf{r}$, where n is the electron density, $\mathbf{p}$ their dipolar moment, e the electron charge and $\mathbf{r}$ the electron displacement. Once the polarization is known, we can determine the value of the dielectric function $\varepsilon(\omega)$ using equations (1) and (3).

2.1.1 Drude-Sommerfeld theory

The Drude-Sommerfeld model for the free-electron gas considers the following equation:

$$m^* \frac{\partial^2 \mathbf{r}}{\partial t^2} + m^* \Gamma \frac{\partial \mathbf{r}}{\partial t} = e\mathbf{E}_0 \mathrm{e}^{-i\omega t}, \tag{4}$$

where e is the charge, m^* is the effective mass of the free electrons, Γ is the damping term, $\mathbf{E}_0$ is the amplitude of the applied electric field and ω is the frequency of that same field. The electron displacements induced by the external field are $\mathbf{r}(t) = \mathbf{r}_0 \mathrm{e}^{-i\omega t}$, and applying equations (1) and (3), it is obtained:

$$\varepsilon_{Drude}(\omega) = 1 - \frac{\omega_p^2}{\omega^2 + i\Gamma\omega}. \tag{5}$$

In this equation, the volume plasma frequency $\omega_p = \sqrt{ne^2/(m^*\varepsilon_0)}$ is introduced. The expression (5) can also be separated into real and imaginary parts as follows:

$$\varepsilon_{Drude}(\omega) = 1 - \frac{\omega_p^2}{\omega^2 + \Gamma^2} + i\frac{\Gamma\omega_p^2}{\omega(\omega^2 + \Gamma^2)}. \tag{6}$$

We proceed to plot the previous equation (6) to obtain the graphical representation of the dielectric function for gold, using $\omega_p = 13.8 \times 10^{15}$ s^{-1} and $\Gamma = 1.075 \times 10^{14}$ s^{-1} [17]. As we can see in Figure 5, the real part of the dielectric function is negative. Consequently,

this negative permittivity leads to a strong imaginary part of the refractive index, and therefore light barely can penetrate a metal. The imaginary part of the dielectric constant describes the dissipation of energy associated with the motion of electrons in the metal.

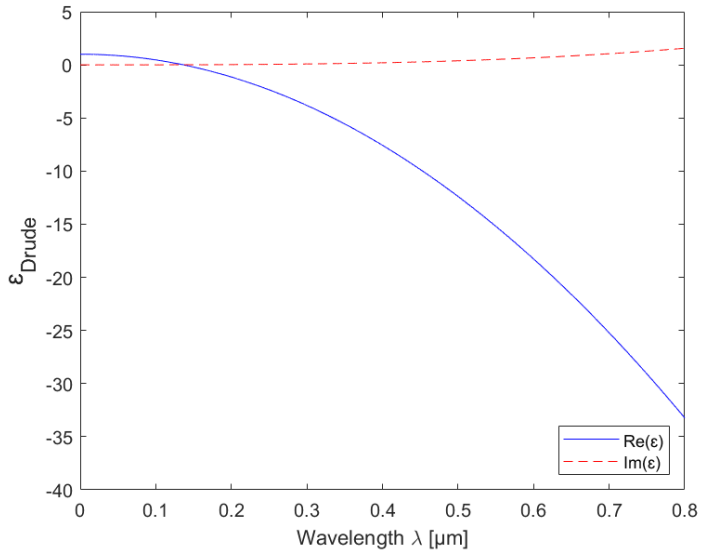

Figure 5: Real (solid blue line) and imaginary (dashed red line) part of the dielectric function for gold according to the Drude–Sommerfeld free-electron model.

2.1.2 Lorentz theory

The Drude–Sommerfeld model studied is accurate enough to study the optical properties of metals in the infrared regime. However, in the visible range it needs to be supplemented by the response of bound electrons, since higher-energy photons can promote electrons of lower-lying bands into the conduction band. This model, that incorporates interband transitions through an additional spring term, is known as the Lorentz theory. The equation of motion for bound electrons is then written as:

$$m^* \frac{\partial^2 \mathbf{r}}{\partial t^2} + m^* \Gamma \frac{\partial \mathbf{r}}{\partial t} + \alpha \mathbf{r} = e\mathbf{E}_0 \mathrm{e}^{-i\omega t}, \tag{7}$$

where α is the spring constant of the potential that keeps the electron in place.

Following the same method used in the previous section, but in this case for the bound electrons, we obtain the following result:

$$\varepsilon_{Lorentz}(\omega) = 1 + \frac{\tilde{\omega}_p^2}{(\omega_0^2 - \omega^2) - i\Gamma\omega}. \tag{8}$$

In this equation, $\omega_0 = \sqrt{\alpha/m^*}$ and $\tilde{\omega}_p$, analogous to the volume plasma frequency ω_p, is defined as $\tilde{\omega}_p = \sqrt{\tilde{n}e^2/(m^*\varepsilon_0)}$, with $\tilde{n}$ being the density of bound electrons. As we did in the Drude-Sommerfeld method, we can rewrite this expression (8) to separate it into real and imaginary parts as follows:

$$\varepsilon_{Lorentz}(\omega) = 1 + \frac{\tilde{\omega}_p^2(\omega_0^2 - \omega^2)}{(\omega_0^2 - \omega^2)^2 + \Gamma^2\omega^2} + i\frac{\Gamma\tilde{\omega}_p^2\omega}{(\omega_0^2 - \omega^2)^2 + \Gamma^2\omega^2}. \tag{9}$$

We represent equation (9) to show the contribution of bound electrons to the dielectric function of gold, using $\tilde{\omega}_p = 45 \times 10^{14}$ s^{-1}, $\Gamma = 9 \times 10^{14}$ s^{-1} and $\omega_0 = 2\pi c/\lambda$, with $\lambda = 450$ nm [17].

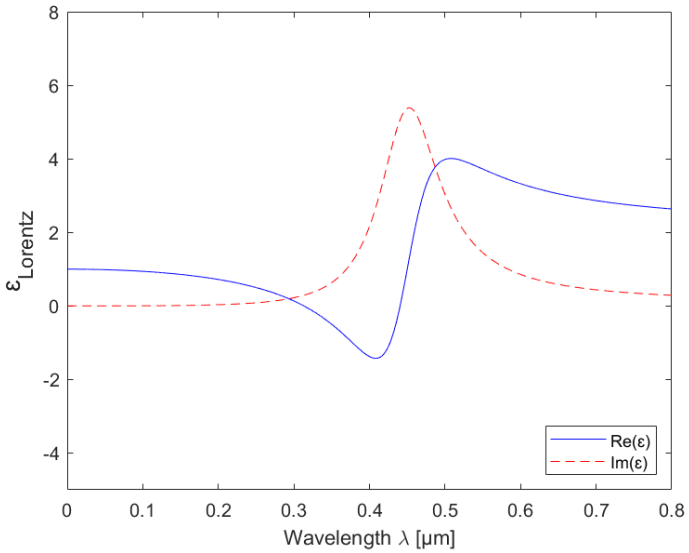

Figure 6: Contribution of bound electrons to the dielectric function of gold, according to the Lorentz model. The solid blue line is the real part and the dashed red curve is the imaginary part of the dielectric function associated with bound electrons.

In Figure 6 it can clearly be observed the resonant behavior of the imaginary part and the dispersion-like behavior for the real part. Moreover, it can also be seen that interband transitions become significant for wavelengths below 0.65 μm.

2.2. Dispersion relation of SPPs at a single interface

The dispersion relation of surface plasmon polaritons (SPPs) at a single interface is the relationship between the frequency of the SPP and its wave vector. In order to describe the properties of SPPs and to obtain the dispersion relation, we have to apply Maxwell's equations and the boundary conditions at the interface between a conductor and a dielectric [15].

2.2.1 Wave equation

In the absence of external charge and current densities, we use the following equation derived from Maxwell's equations as starting point:

$$\bigtriangledown \times \bigtriangledown \times \mathbf{E} = -\mu_0 \frac{\partial^2 \mathbf{D}}{\partial t^2}. \tag{10}$$

Considering $\varepsilon = \varepsilon(\mathbf{r})$ over distances on the order of one optical wavelength, the central equation of electromagnetic wave theory is the following one:

$$\bigtriangledown^2 \mathbf{E} - \frac{\varepsilon}{c^2} \frac{\partial^2 \mathbf{E}}{\partial t^2} = 0. \tag{11}$$

Assuming a harmonic time dependence $\mathbf{E}(\mathbf{r},t) = \mathbf{E}(\mathbf{r})\mathrm{e}^{-i\omega t}$ of the electric field, and defining $k_0 = \frac{\omega}{c}$ as the wave vector of the propagating wave in vacuum, the equation transforms into:

$$\bigtriangledown^2\mathbf{E} + k_0^2\varepsilon\mathbf{E} = 0. \tag{12}$$

We assume that the waves propagate along the x-direction and show no spatial variation in the y-direction (see axis in Figure 4(a)). Therefore, $\varepsilon = \varepsilon(z)$ and the propagating waves can be described as $\mathbf{E}(x,y,z) = \mathbf{E}(z)\mathrm{e}^{i\beta x}$, where $\beta = k_x$ is the propagation constant of the traveling wave. With these assumptions, the equation (12) transforms into:

$$\frac{\partial^2\mathbf{E}(z)}{\partial z^2} + (k_0^2\varepsilon - \beta^2)\mathbf{E} = 0. \tag{13}$$

Obviously, there is an analogous equation for the magnetic field. The system of equation obtained by applying Maxwell's curl equations with the assumed field dependence is:

$$\frac{\partial E_y}{\partial z} = -i\omega\mu_0 H_x \tag{14}$$

$$\frac{\partial E_x}{\partial z} - i\beta E_z = i\omega\mu_0 H_y \tag{15}$$

$$i\beta E_y = i\omega\mu_0 H_z \tag{16}$$

$$\frac{\partial H_y}{\partial z} = i\omega\varepsilon_0\varepsilon E_x \tag{17}$$

$$\frac{\partial H_x}{\partial z} - i\beta H_z = -i\omega\varepsilon_0\varepsilon E_y \tag{18}$$

$$i\beta H_y = -i\omega\varepsilon_0\varepsilon E_z. \tag{19}$$

This system allows two sets of solutions with different polarization properties of the propagating waves. The first set is the transverse electric (TE or s) modes, with only H_x, H_z and E_y being nonzero, and the second set is the transverse magnetic (TM or p) modes, where only E_x, E_z and H_y are nonzero.

The most simple structure that sustains SPPs, shown in Figure 4(a), is the single interface between a dielectric ($z > 0$) with positive real dielectric constant ε_2 and a metal ($z < 0$) described by a dielectric function $\varepsilon_1(\omega)$, that has to fulfill $\mathrm{Re}[\varepsilon_1] < 0$. Moreover, as we want the propagating wave solutions to be confined to the interface, they have to be written with evanescent decay in the z-direction.

For TE modes, the obtained solutions are:

For $z < 0$:

$$E_y(z) = A_1\mathrm{e}^{i\beta x}\mathrm{e}^{k_1 z} \tag{20}$$

$$H_x(z) = iA_1\frac{1}{\omega\mu_0}k_1\mathrm{e}^{i\beta x}\mathrm{e}^{k_1 z} \tag{21}$$

$$H_z(z) = A_1\frac{\beta}{\omega\mu_0}\mathrm{e}^{i\beta x}\mathrm{e}^{k_1 z} \tag{22}$$

For $z > 0$:

$$E_y(z) = A_2 \mathrm{e}^{i\beta x} \mathrm{e}^{-k_2 z} \tag{23}$$

$$H_x(z) = -iA_2 \frac{1}{\omega\mu_0} k_2 \mathrm{e}^{i\beta x} \mathrm{e}^{-k_2 z} \tag{24}$$

$$H_z(z) = A_2 \frac{\beta}{\omega\mu_0} \mathrm{e}^{i\beta x} \mathrm{e}^{-k_2 z} \tag{25}$$

Continuity of E_y and H_x at the interface leads to the condition:

$$A_1(K_1 + K_2) = 0. \tag{26}$$

In order to fulfill $\mathrm{Re}[k_1] > 0$ and $\mathrm{Re}[k_2] > 0$ (evanescent field in z direction), the only possible solution is $A_1 = A_2 = 0$. Therefore, no surface modes exist for TE polarization. As we will demonstrate in the next steps, SPPs only exist for TM polarization.

For TM modes, the solutions are:

For $z < 0$:

$$H_y(z) = A_1 \mathrm{e}^{i\beta x} \mathrm{e}^{k_1 z} \tag{27}$$

$$E_x(z) = -iA_1 \frac{1}{\omega\varepsilon_0\varepsilon_1} k_1 \mathrm{e}^{i\beta x} \mathrm{e}^{k_1 z} \tag{28}$$

$$E_z(z) = -A_1 \frac{\beta}{\omega\varepsilon_0\varepsilon_1} \mathrm{e}^{i\beta x} \mathrm{e}^{k_1 z} \tag{29}$$

For $z > 0$:

$$H_y(z) = A_2 \mathrm{e}^{i\beta x} \mathrm{e}^{-k_2 z} \tag{30}$$

$$E_x(z) = iA_2 \frac{1}{\omega\varepsilon_0\varepsilon_2} k_2 \mathrm{e}^{i\beta x} \mathrm{e}^{-k_2 z} \tag{31}$$

$$E_z(z) = -A_2 \frac{\beta}{\omega\varepsilon_0\varepsilon_2} \mathrm{e}^{i\beta x} \mathrm{e}^{-k_2 z} \tag{32}$$

Continuity of H_y and $\varepsilon_i E_z$ at the interface requires that $A_1 = A_2$ and

$$\frac{k_2}{k_1} = -\frac{\varepsilon_2}{\varepsilon_1}. \tag{33}$$

Moreover, H_y has to fulfill the corresponding wave equation for TM modes, that is analogous to equation (13) for the electric field, considering only the y component of $\mathbf{H}$. From that, it is obtained:

$$k_1^2 = \beta^2 - k_0^2\varepsilon_1 \tag{34}$$

$$k_2^2 = \beta^2 - k_0^2\varepsilon_2. \tag{35}$$

Combining these two equations with equation (33), we finally arrive to the dispersion relation of SPPs propagating at a single interface between the dielectric and the metal, that can be written as:

$$\beta = k_0 \sqrt{\frac{\varepsilon_1 \varepsilon_2}{\varepsilon_1 + \varepsilon_2}}, \tag{36}$$

where β is the wave vector of the SPP, k_0 is the wave vector of the incident light in free space, ε_1 is the dielectric constant of the metal, and ε_2 is the dielectric constant of the dielectric material.

2.2.2 Dispersion relation

The dispersion relation, equation (36), shows that the wave vector of the SPP is directly proportional to the frequency of the incident light and is dependent on the dielectric properties of the metal and the dielectric. It also shows that the SPP wave vector is larger than the wave vector of the incident light in free space, i.e., the wavelength is shorter. The dispersion relation is important for understanding the behavior of SPPs at the interface and for designing structures that can support SPPs with specific frequencies and wave vectors.

We discuss two descriptions for the metal: the pure Drudre-Sommerfeld dielectric function, given by equation (6), and the more realistic dielectric function that includes interband transitions, given by the Lorentz model, written in equation (9). For both cases, we neglect the damping of the surface wave in the x-direction, and therefore we only consider the real part of ε_2. In Figure 7 we plot this dispersion relation for a metal, in this case gold, with negligible damping, described by the real Drude dielectric function for an gold-air (ε_2=1) interface. Both real and imaginary parts of the wave vector β are shown, normalized to the plasma frequency ω_p and multiplied by the speed of light in the vacuum, c. The frequency ω is also normalized to ω_p. In Figure 8 we compare that dispersion relation with the one obtained at a gold/silica (ε_2=2.25) interface.

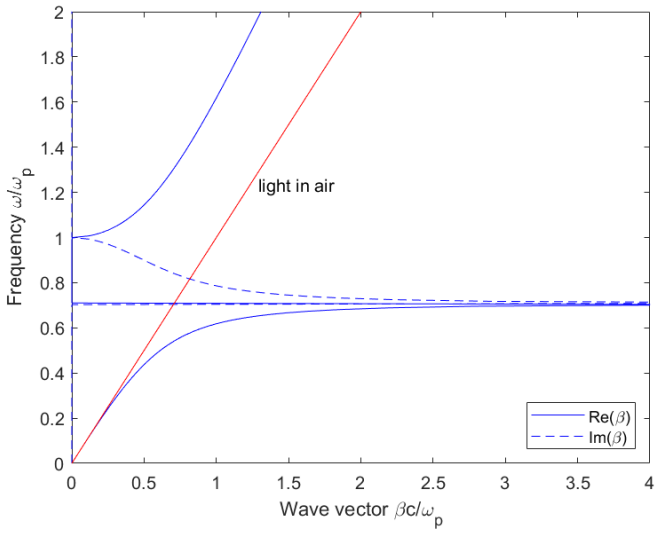

Figure 7: Dispersion relation of SPPs at a gold/air interface according to the Drude–Sommerfeld free-electron model. In this plot, the frequency ω and the wave vector β are normalized to the plasma frequency ω_p, and both the real (blue continuous curves) and the imaginary part (blue dashed curves) of the wave vector are shown. The red line corresponds to the light line in air.

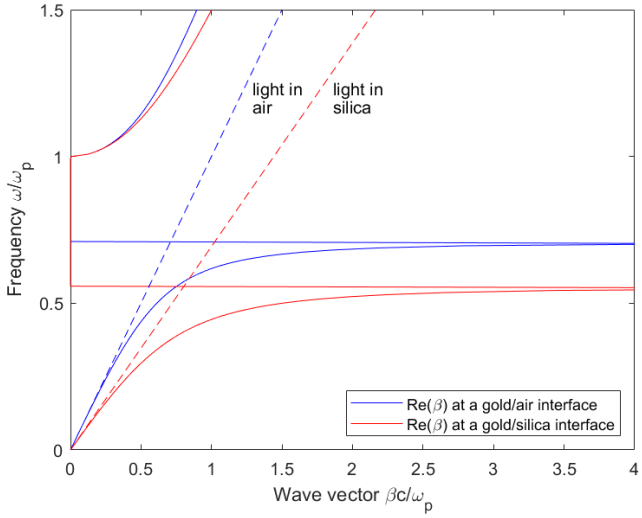

Figure 8: Dispersion relation of SPPs at the interface between gold and air (blue curves) and silica (red curves), according to the Drude–Sommerfeld free-electron model. In this plot, the frequency ω and the wave vector β are normalized to the plasma frequency ω_p, and only the real part (continuous curves) of the wave vector is shown. The dashed lines are the light lines in air and silica.

The real part of the wave vector β determines the SPP wavelength, while the imaginary part accounts for the damping of the SPP as it propagates along the interface. For small wave vectors corresponding to low frequencies, the SPP propagation constant is close to k_0 at the light line (red line in Figure 7), $\omega = ck$. However, for large wave vectors, the frequency of the SPPs approaches the characteristic surface plasmon frequency ω_{sp}, that can be obtained by inserting the Drude-Sommerfeld equation (5) into the dispersion equation (36).

$$\omega_{sp} = \frac{\omega_p}{\sqrt{1+\varepsilon_2}}. \tag{37}$$

In Figures 7 and 8 we have studied the case of a gold/air (ε_2=1) interface, therefore the equation (37) transforms into $\omega_{sp} = \omega_p/\sqrt{2}$.

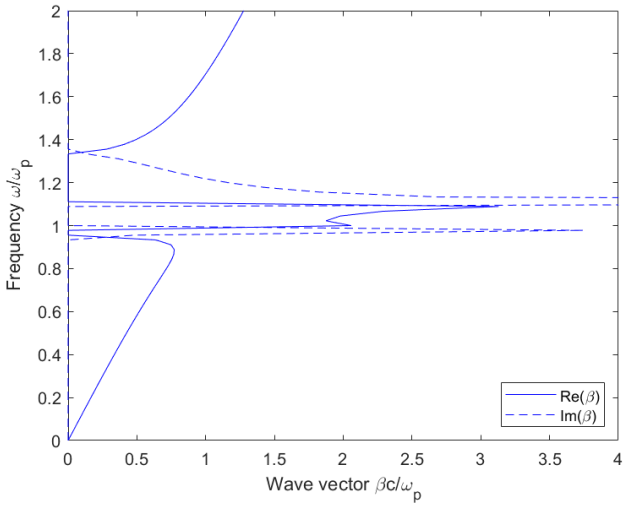

Figure 9: Dispersion relation of SPPs at a gold/air interface, according to the Lorentz model. In this plot, the frequency ω and the wave vector β are normalized to the plasma frequency ω_p, and both the real (continuous curves) and the imaginary part (dashed curves) of the wave vector are shown.

Figure 9 shows the dispersion relation of SPPs propagating at a gold/air interface, with the dielectric function of gold considering also the interband transitions. Compared with the dispersion relation of completely undamped SPPs shown in Figure 7, it can be seen that the bound SPPs approach now a maximum, finite wave vector at the surface plasmon frequency ω_{sp} of the system.

In order to excite plasmons, the incident light must couple to surface charges. Graphically, this means that the light line has to be crossed by the dispersion curve of the SPP. Although this already happens in the interval between ω_{sp} and ω_p, we want it to occur where the absorption is not that big. Therefore, the goal is to excite plasmons in the $\omega < \omega_{sp}$ range by modifying the line of the incident light. Consequently, the wave vector component of the exciting light has to be increased over its free-space value. There is a wide variety of methods to achieve this increase of the wave vector component. For instance, the most simple one is creating evanescent waves at the interface between a medium with refractive index $n > 1$, therefore the obtained light line is $\omega = ck/n$ [17]. Some possible experimental arrangements are shown in Figure 10.

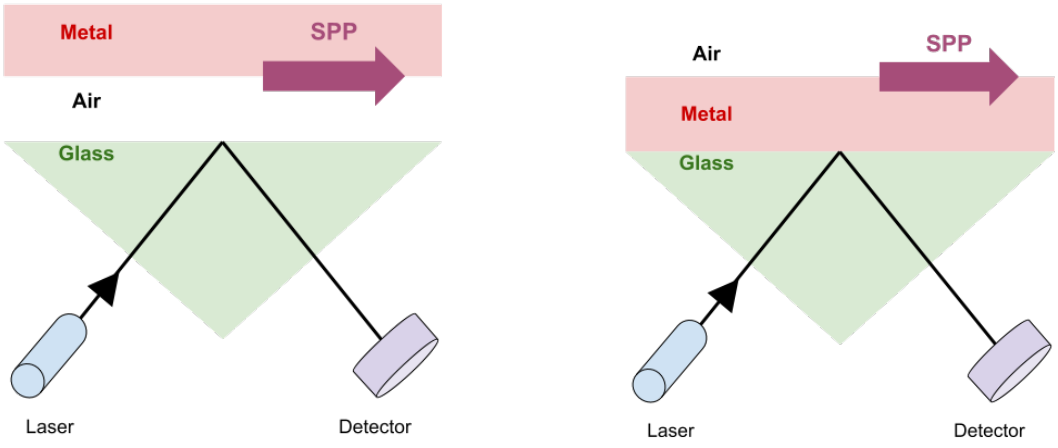

(a) (b)

Figure 10: Experimental arrangements to excite surface plasmons. 10(a): Otto configuration. 10(b): Kretschmann configuration.

In the Otto configuration [18], shown in Figure 10(a), the tail of an evanescent wave at a glass/air interface is brought into contact with a metal/air interface that supports SPPs. If the separation between the two interfaces is large enough, the evanescent wave is only weakly influenced by the presence of the metal. By tuning the angle of incidence of the totally reflected beam inside the prism, the resonance condition for excitation of SPPs can be fulfilled. The excitation of a SPP will show up as a minimum in the reflected light.

However, the Otto configuration proved to be experimentally inconvenient because of the challenge of controlling the tiny air gap between the two interfaces. In 1971, Kretschmann came up with an alternative method to excite SPPs that solved this problem [19]. In his method, a prism deposited below a thin metal film is used in the full-internal reflection regime, as it can be seen in Figure 10(b).

To excite a surface plasmon at the metal/air interface an evanescent wave created at the glass/metal interface has to penetrate through the metal layer.

Another possibility is to use a periodic structure (grating) [20]. Considering a dielectric/metal interface that supports surface plasmons, if we periodically perturb the dielectric surface, the surface mode between the dielectric and the metal will not be just a single inhomogeneous plane wave but an infinite series of Floquet harmonics with the wavenumbers $k_{tn} = k_t + n\frac{2\pi}{D}$, where $n = \pm 1, 2, ..$ and D is the perturbation period. Properly selecting the period, it is possible to ensure that one of these harmonics is in phase with the incident plane wave, i.e., k_{tn} is equal to the tangential component of the wave vector of the incident propagating plane wave.

3. Spintronic-plasmonic metasurfaces

Spintronic-plasmonic metasurfaces are metallic or dielectric structures that combine the properties of plasmons and electron spin to achieve unique optical and electronic properties, due to the Magneto-refractive effect (MRE), which is responsible for the variation in the optical constants of a spintronic system caused by the change in the electrical resistivity, that is induced by the magnetic field.

In a spintronic-plasmonic metasurface, the metallic structures are designed to support Surface Plasmon Polaritons (SPPs) or Localized Surface Plasmons (LSPs) confined in nanoparticles acting as nanoantennas at the metal-dielectric interface that we have studied in the previous chapter. These SPPs can interact with the spin properties of the electrons, leading to spin-dependent optical properties. For example, by controlling the magnetization direction of a ferromagnetic layer in a spintronic-plasmonic metasurface with an external magnetic field, it is possible to tune the transmission of light.

3.1. Giant Magnetoresistance (GMR)

The Giant Magnetoresistance (GMR) is a quantum mechanical effect that occurs in thin film structures composed of alternating ferromagnetic and non-magnetic layers. The effect manifests as a significant change in the electrical resistance in the presence of a magnetic field, depending on whether the magnetization of adjacent ferromagnetic layers are in a parallel (P) or an antiparallel (AP) alignment, as it can be seen in Figure 11.

The direction of this magnetization can be controlled by applying an external magnetic field **H**. In the absence of a magnetic field, the alignment of the magnetization of the adjacent ferromagnetic layers is antiparallel and the electrical resistance much higher than in the presence of a magnetic field, where the alignment of the ferromagnetic layers is parallel and the resistance is relatively low [21].

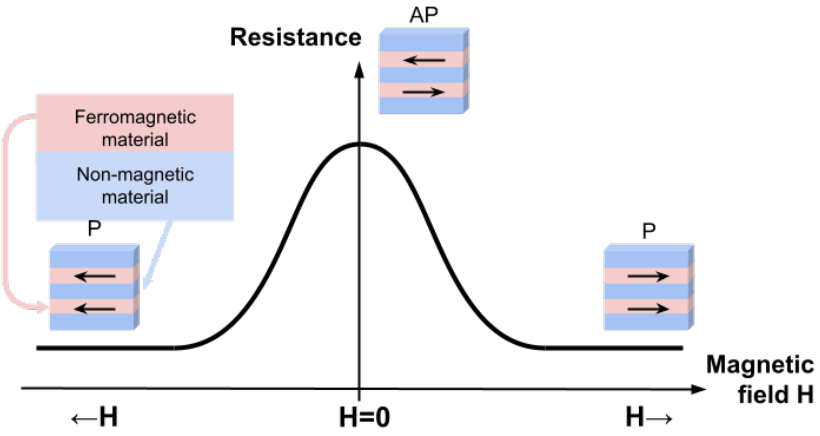

Figure 11: Schematic representation of the magnetic field dependence of the resistance of a GMR multilayer. The GMR multilayer is composed of alternating layers of non-ferromagnetic and ferromagnetic metals. When the magnetization of the adjacent ferromagnetic layers is antiparallel (AP), the resistance is much higher than when the magnetization of the ferromagnetic layers is parallel (P).

The GMR was first reported for the Fe/Cr/Fe system in 1988, when the relative orientation of the magnetization of the individual Fe layers switched from antiparallel to parallel state by applying an external magnetic field and the electrical resistivity changed considerably [22]. This change only occurred for specific Cr thickness, for which the adjacent Fe layers are antiparallel. This antiparallel orientation of the magnetization of the adjacent Fe layers can be switched to parallel orientation by the application of a large enough external magnetic field.

The relative change of the resistivity is defined as follows:

$$\frac{\delta\rho}{\rho} = \frac{\rho(H) - \rho(no\ H)}{\rho(no\ H)} = \frac{\rho_P - \rho_{AP}}{\rho_{AP}}, \tag{38}$$

where ρ_{AP} is the resistivity of the antiparallel state, and therefore when there is no magnetic field applied, and ρ_P is the resistivity of the parallel state, i.e., when there is an external magnetic field applied. Alternative forms of this expression may use electrical resistance instead of resistivity, and are sometimes normalized by ρ_P rather than ρ_{AP}.

The change in the resistivity of the GMR systems can be understood considering that the main scattering mechanisms are spin-conserving and that the electrical conductivity is the sum of the conductivity of majority (spin up) and minority (spin down) electrons. In Figure 12 a schematic representation shows the energy dependence of the Density of States (DOS) for the parallel state (P), split into localized electrons (responsible for the magnetization) and delocalized or conduction electrons (responsible for the electric conductivity).

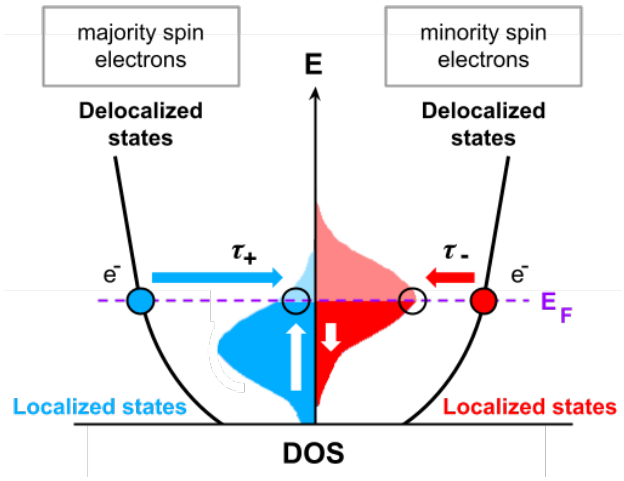

Figure 12: Schematic representation of the Density of States (DOS) of a GMR multilayer in the P state for different types of electrons.

The DOS of the localized electrons is different for spin up and spin down electrons, due to the exchange interaction. Besides, the localized states of the spin up electrons are nearly all occupied, whereas the spin down localized states are partially occupied. However, the DOS of the delocalized electrons is very similar for both spins. At the Fermi energy, the scattering time of these conduction electrons depends on the number of states available for scattering which, due to the occupation of the localized band, is different for the spin up and spin down electrons.

Consequently, for the P state we obtain a much higher conductivity (and therefore a lower resistivity) for the spin up current than for the spin down current. On the other hand, for the AP state the conduction electrons are indistinguishable, which results in a symmetrization of the available scattering channels and, therefore, an increase of the resistivity.

The main application of GMR multilayer structures is in magnetic field sensors, which are used to read stored data in hard disk drives, by measuring the change in electrical resistance of the GMR device in response to the magnetic field from the disk. GMR systems have also been extensively used for biosensors, microelectromechanical systems (MEMS) and other devices [23]. Moreover, they are used in magnetoresistive random-access memory (MRAM) as cells that store one bit of information.

3.2. The Magneto-refractive effect (MRE)

The Magneto Optic (MO) effect is a phenomenon in which the optical properties of a material are influenced by the presence of a magnetic field [24]. These phenomena were first discovered by Michael Faraday in 1845 [25]. He noticed that the polarization of a linearly polarized light beam is rotated when it propagates parallel to an externally applied magnetic field. This discovery initiated a research for materials showing optical cross effects, in which the polarization or the intensity of the light beam can be manipulated via external fields.

The Magneto-refractive effect (MRE) is a specific type of MO effect defined as the change in the refractive index of a material, such as a GMR magnetic multilayer, in the presence of a magnetic field due to the variations in the electrical resistivity and conductivity. In fact, the MRE was discovered in GMR multilayers by Jacquet and Valet in 1995 [8]. They found out that the change in the resistance as a consequence of the GMR directly implied a change in the refractive index of the system, and that change was more evident in spectral regions where interband transitions were absent (IR region). The spin dependent conduction electron transport inherent to GMR manifests directly in the optical properties from the NIR all the way to the THz range, where the contribution to the optical properties of conduction electrons dominate.

The MRE can be applied to optically probe, without the need of electrical contacts, the magnetotransport properties of a number of materials systems and spintronic devices in the infrared and optical ranges, as well as to get a deeper understanding of the spin polarized electron properties of ferromagnets.

3.2.1 MRE in GMR systems

The Magneto-refractive effect plays a key role in GMR systems. It has recently been demonstrated that metamaterial platforms based on GMR multilayers allow for mid-IR modulation under very weak magnetic fields of around 3 mT. As explained before, and also as it is schematically represented in Figure 13(a), when a magnetic field is applied to a GMR multilayer, the magnetic moments of the ferromagnetic layer become aligned with respect to those of the adjacent layers, leading to changes in the electrical resistance, and therefore in the electrical conductivity.

However, in addition to these changes in the electrical resistance, and as it is shown in Figure 13(b), the MRE also causes variations in the optical properties, because the magnetic field can modify the refractive index of the ferromagnetic layer. Therefore, the variation in the dielectric constant induced by the magnetic field can be determined by measuring the reflection and transmission of light under a magnetic field. These changes in the reflectivity ($\Delta R/R$) and transmissivity ($\Delta T/T$) are due to changes in the real ($\Delta\varepsilon_r$) and imaginary ($\Delta\varepsilon_i$) parts of the dielectric constant [26].

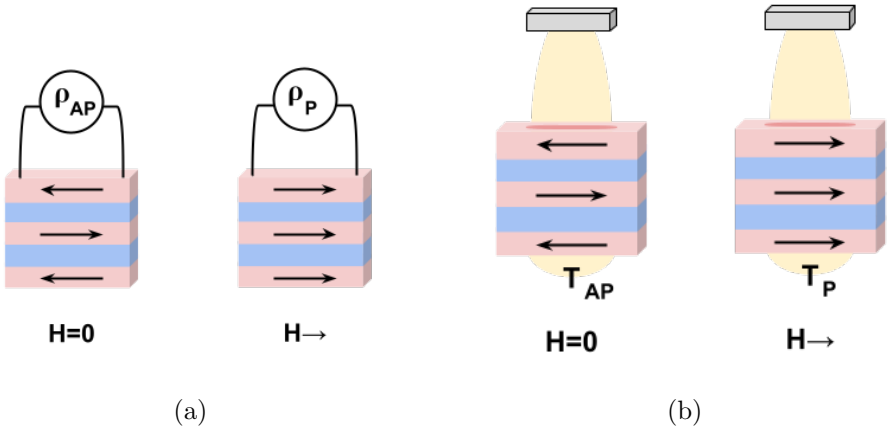

Figure 13: Schematic representation of the connection between Spintronics and Plasmonics by the MRE. (a) An external magnetic field **H** reorients the individual layer magnetizations from antiparallel to parallel configurations, with the subsequent change in the electrical resistivity (GMR). (b) The magnetic field-induced change in resistivity produces a change in the mid- and far-IR optical properties (MRE) dominated by conduction electrons (T_P and T_{AP} correspond to the light trasnmission when the layer magnetizations are oriented parallel or antiparallel, respectively).

The optical response of the system can be described either by the dielectric tensor $\varepsilon(\omega)$ (or complex refractive index, $\varepsilon = (n + ik)^2$) or by the conductivity $\sigma(\omega)$. Both tensors are related in the following way [22]:

$$\varepsilon(\omega) = 1 + i\frac{\sigma(\omega)}{\omega}, \tag{39}$$

that is why the very same electron conduction mechanism is responsible for both the electron transport and optical response. It has been proved that, despite the fact that interband transitions may play a role, an accurate description of the MRE can be obtained taking only into account the contributions of conduction electrons. Therefore, the conductivity can be split into two parts, each one corresponding to one of the two spin orientations.

When there is an external magnetic field applied, all the magnetic moments of the layers are oriented parallel (Figure 14) and the conductivity can be written as the sum of the two spin channels. Accordingly, the conductivity can be expressed as the addition of the conductivity of the electrons whose spin is parallel to the total magnetization, $\sigma_+(\omega)$, and the conductivity of the electrons whose spin is antiparallel (-) to the total magnetization, $\sigma_-(\omega)$:

$$\sigma_P(\omega) = \sigma_+(\omega) + \sigma_-(\omega). \tag{40}$$

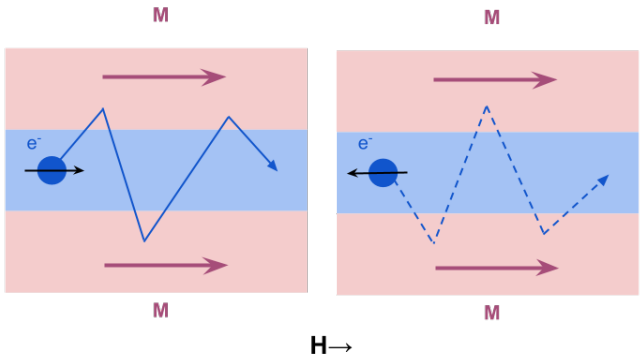

Figure 14: Schematic representations of the spin dependent scattering processes in the multilayer. Under the application of an external magnetic field **H**, the magnetizations **M** of the layers orient parallel to each other. The blue dots represent the conduction electrons and the thin arrow of each electron refer to its spin. In this situation, the scattering of the electrons with spin parallel to M (solid blue line) is different to the scattering of the electrons with spin antiparallel to M (dotted blue line).

However, for antiparallel orientation of the magnetizations (Figure 15), since the electrons of both spin channels are indistinguishable, the system behaves as a spinless conduction electron gas and the conductivity can be expressed as:

$$\sigma_{AP}(\omega) = \frac{e^2}{(1 - i\omega\tau)} \frac{n}{m^*}. \tag{41}$$

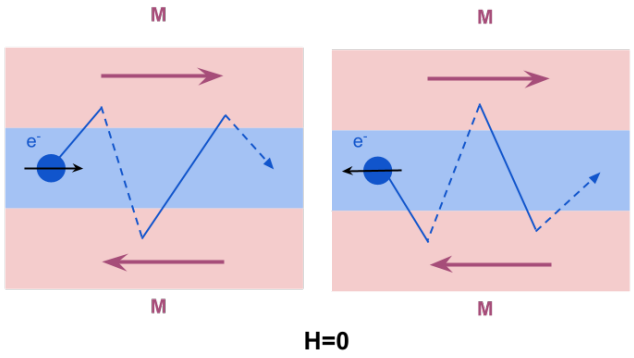

Figure 15: Schematic representations of the spin dependent scattering processes in the multilayer. When no external magnetic field **H** is applied, the magnetizations **M** of the layers assumes an antiparallel arrangement. The blue dots represent the conduction electrons and the thin arrow of each electron refer to its spin. In this situation, the conduction electrons are indistinguishable and the scattering (both solid and dotted blue lines) is the same for both electrons.

The conductivities $\sigma_{+,-}(\omega)$ for the parallel state are described as:

$$\sigma_{+,-}(\omega) = \frac{e^2}{(1 - i\omega\tau_{+,-})} \frac{n_{+,-}}{m^*_{+,-}}, \tag{42}$$

where $\tau_{+,-} = 1/\Gamma_{+,-}$ are the relaxation times of the spin channels and $n_{+,-}/m^*_{+,-}$ the ratio between the electron densities and the effective mass of the conduction electrons.

It can easily be proved that:

$$\sigma_{AP}(\omega) = \frac{4\sigma_+(\omega)\sigma_-(\omega)}{\sigma_+(\omega) + \sigma_-(\omega)}. \tag{43}$$

Both key properties can be expressed in terms of two parameters α and β :

$$\tau_{+,-}(\omega) = \frac{\tau_0}{1 \pm \beta} \tag{44}$$

$$\frac{n_{+,-}}{m^*_{+,-}} = \frac{n}{2m^*(1 \pm \alpha)}, \tag{45}$$

where τ_0 is the relaxation time, n the total conduction electron density and m^* the electron effective mass. In these equations, β reflects the asymmetry in the relaxation times and α represents the variation in the electron densities and effective masses for the two spin states.

The dielectric constant of the GMR multilayer is determined by the electron conductivity. Applying the equation (39) and using the previously obtained equations for both $\sigma_P(\omega)$ and $\sigma_{AP}(\omega)$, the effective dielectric functions for the parallel and antiparallel states can be written in the following way:

$$\varepsilon_P(\omega) = 1 + i\frac{\omega_P^2}{2\omega}\left[\left(\frac{1}{1+\alpha}\right)\left(\frac{1}{\Gamma_0(1+\beta) - i\omega}\right) + \left(\frac{1}{1-\alpha}\right)\left(\frac{1}{\Gamma_0(1-\beta) - i\omega}\right)\right] \tag{46}$$

$$\varepsilon_{AP}(\omega) = 1 + i\frac{\omega_P^2}{\omega}\left(\frac{1}{\Gamma_0(1+\alpha\beta) - i\omega}\right), \tag{47}$$

where ω_p is the plasmon frequency ($\omega_p^2 = e^2 n/m^*$) and $\Gamma_0 = 1/\tau_0$.

In the P state, the two terms between brackets in equation (46) reflect the contribution of the two spin channels, which have different damping factors, $\Gamma_0(1+\beta)$ and $\Gamma_0(1-\beta)$. On the contrary, in the AP state, since the spin up and down are indistinguishable, the equation (47) describes a spin-less conduction electron system with an effective damping factor of $\Gamma_{eff} = \Gamma_0(1+\alpha\beta)$. This last equation is also used to describe structures that show no GMR effect. In that case, both α and β are zero, and for that reason the damping factor is simply $\Gamma_{eff} = \Gamma_0$. Therefore, $\varepsilon_{AP}(\omega)$ can be used to obtain the effective dielectric permittivity at $\mathbf{H} = 0$.

The effective dielectric tensor [8] that describes the optical behaviour of the whole system of the GMR multilayer under the application of a magnetic field is written in the following way:

$$\overline{\varepsilon} = \begin{pmatrix} \varepsilon_H(\omega) & 0 & 0 \\ 0 & \varepsilon_H(\omega) & 0 \\ 0 & 0 & \varepsilon_{no\ H}(\omega) \end{pmatrix} = \begin{pmatrix} \varepsilon_P(\omega) & 0 & 0 \\ 0 & \varepsilon_P(\omega) & 0 \\ 0 & 0 & \varepsilon_{AP}(\omega) \end{pmatrix}, \tag{48}$$

where ε_H is the dielectric function when a magnetic field is applied and therefore the GMR multilayers are in parallel state, ε_P, and $\varepsilon_{no\ H}$ is the dielectric constant when there is no applied magnetic field and the GMR multilayers are in antiparallel state, ε_{AP}.

In almost all the GMR systems the strength of the magnetic field needed to change the relative orientation of the magnetization of the ferromagnetic layers (from AP to P states) is in the range of KOe (1 KOe=0.1 T). However, in the $Ni_{81}Fe_{19}$/Au multilayer system, MRE can be obtained at very low magnetic fields (a few tens of Oe). Henceforward, the modelled system is going to be a thick film of the $Ni_{81}Fe_{19}$/Au multilayer on a CaF_2 substrate surrounded by air, as shown in Figure 16(a). The difference in the Au thicknesses of the multilayers results in different values of the GMR, such as 4% GMR for 2.3 nm thick Au layers and 0.8% GMR for 3.3 nm thick Au layers.

In Figure 16(b) we present the curves of the calculated dielectric permittivity, ε_{AP}, for a system of $Ni_{81}Fe_{19}$/Au multilayers for different values of Au thicknesses, and therefore different values of GMR, achieved by changing the values of the plasmon frequency and the damping factor (ω_P, Γ_{eff}). More precisely, the selected values of Au thickness to plot are 1.9 nm (0% GMR), 2.3 nm (4% GMR) and 3.3 nm (0.8% GMR), which have (ω_P, Γ_{eff}) values of (5.3 eV, 70 meV), (5.5 eV, 75 meV) and (5.8 eV, 75 meV) respectively, obtained from [26].

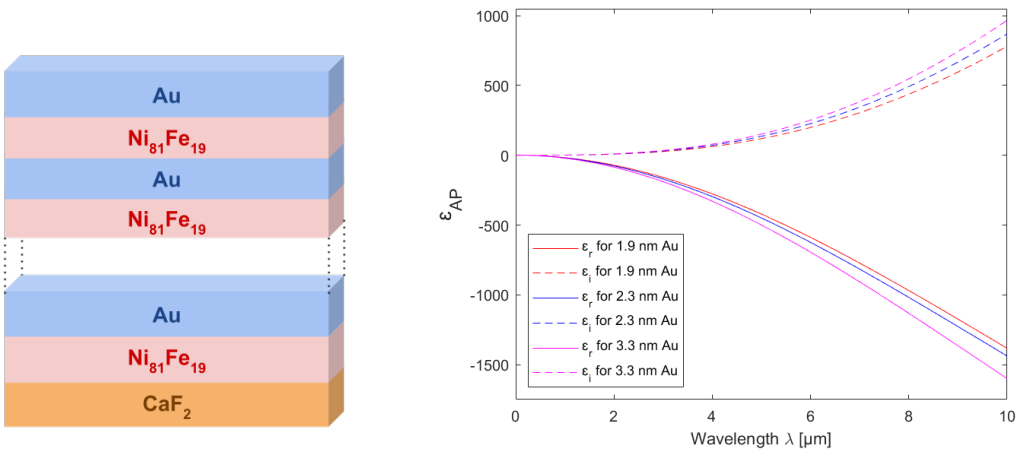

(a) (b)

Figure 16: (a) Schematic representation of the GMR system of $Ni_{81}Fe_{19}$/Au multilayers on a CaF_2 substrate embedded in air. (b) Spectra of the real (continuous line) and imaginary (dashed line) parts of the effective dielectric permittivity, ε_{AP}, calculated for three multilayers with different Au thicknesses, and therefore different values of (ω_P, Γ_{eff}).

The MRE-induced changes (or magnetic modulation) of the dielectric constant are given by the difference:

$$\Delta\varepsilon = \varepsilon_P(\omega) - \varepsilon_{AP}(\omega), \tag{49}$$

which depends, not only on ω_p and Γ_0, but also on the spin related parameters (α, β).

First, we graphically represent in Figure 17 this difference for the 2.3 nm Au (4% GMR) and 3.3 nm Au (0.8% GMR) samples, which, according to [26], correspond to the theoretical values of $(\omega_P, \Gamma_0, \alpha, \beta)$ of (5,5 eV, 0.75 meV, -0.05, 0.245) and (5.8 eV, 75 meV, -0.03, 0.119), respectively. Then, we graphically represent the same equation (49) in Figure 18 for ω_p=5.5 eV, Γ_0=75 meV, and for different values of (α, β) that give a value of GMR of 4%: (0,0.197), (-0.025,0.221) and (-0.05,0.245).

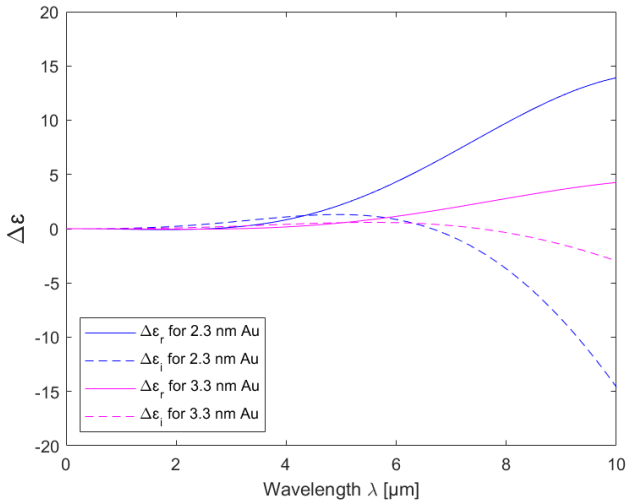

Figure 17: Magnetic modulation of the dielectric constants, $\Delta\varepsilon$, (continuous lines: real part; dashed lines: imaginary part) for two multilayers. The pink lines represent the multilayer with 0.8% GMR (3.3 nm Au), and the blue lines represent a multilayer with 4% GMR (2.3 nm Au).

In Figure 16(b) we present the effective permittivity for the same $Ni_{81}Fe_{19}$/Au multilayers. As it can be observed the effective dielectric constants are very similar. However, it is noticeable in Figure 17 that the magnetic modulation of the effective dielectric constant for the two GMR multilayers is very different. In particular, the intensity of such modulation increases as we increase the GMR value of the multilayer.

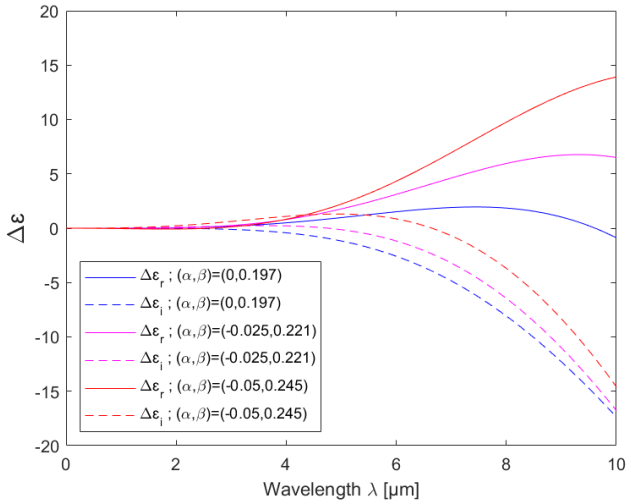

Figure 18: Magnetic modulation of the dielectric constants, $\Delta\varepsilon = \varepsilon_P - \varepsilon_{AP}$ (continuous lines: real part; dashed lines: imaginary part) for three multilayers with 4% GMR with different values of (α, β).

As it shown in both Figures 17 and 18, in the 2 to 4-5 µm spectral range the modifications of the dielectric constants are small. On the other hand, above 5 µm the real part increases, whereas the imaginary part becomes negative and its absolute value shows a monotonic increase with wavelength. Moreover, it can also be observed in Figure 18 that the spectral dependence of the MRE induced changes depends strongly on the values of (α, β), and therefore on the spin asymmetry of the relaxation time and the different electron concentration.

The magneto-refractive effect causes a change in the transmission and the reflection of light when the magnetization directions of the ferromagnetic layers are changed from an antiparallel to a parallel configuration, i.e., when we apply an external magnetic field [27]. This results in a relative transmission change (or modulation of the transmissivity) of:

$$\frac{\Delta T}{T} = \frac{T_P - T_{AP}}{T_{AP}}. \tag{50}$$

The equation for the relative reflection change is analogous to the equation (50) for the transmission.

The analytic expression of the transmission, i.e. the ratio of the transmitted and incident power, can be retrieved by calculating the electromagnetic field on a plane placed below the CaF_2 surface and integrating the time-averaged Poynting vector on it [9]:

$$T = \frac{\int_A \frac{1}{2} Re\left\{\mathbf{E}^* \times \mathbf{H}\right\} \cdot \hat{n}\, dA}{P_0}, \tag{51}$$

where A is the area of the plane, P_0 the power of the incident radiation over the same area, $\hat{n}$ the plane-normal unitary vector, $\mathbf{E}$ and $\mathbf{H}$ the electric and magnetic field recorded on the plane, respectively. There are different approaches to obtain the analytical expression of the transmission for thin metal films, given in the Fresnel equations for transmission and reflection of the electromagnetic fields at the interfaces [28], [29], [30], but we calculate them numerically, as described in next section.

The experimental measurement of the MRE involves a simple reflection or transmission measurement of the IR light from the surface of a GMR multilayer, applying magnetic fields of different strength. Transmission measurements are also possible provided that the total thickness of the sample allows the transmission of the light [31]. The equation (50) described before to define the relative change in the transmission and its analogous for the reflection can be used to obtain the numerical value of the MRE. Moreover, this equation is similar to the equation (38) used to obtain the value of the GMR:

$$\text{MRE\%} = \frac{R(H) - R(no\ H)}{R(no\ H)} \times 100 = \frac{R_P - R_{AP}}{R_{AP}} \times 100. \tag{52}$$

4. Simulations of the optical response

In this section, we present the results of the simulations of the optical response of metasurfaces based on GMR multilayers of $Ni_{81}Fe_{19}$/Au to develop an active photonic platform. In order to simulate the system, we use the software for photonoc simulations called *Lumerical* [32], that predicts how light behaves within complex structures by applying the Finite-difference time-domain (FDTD) method.

4.1. Finite-difference time-domain (FDTD) method

The finite-difference time-domain (FDTD) method is a numerical analysis technique used for finding approximate solutions to the associated system of differential equations in order to obtain the electromagnetic field. This method is a direct solution of Maxwell's time-dependent curl equations [33], and it is purely based on the Yee Algorithm, introduced by Yee in 1966 [34]. Since it is a time-domain method, FDTD solutions can cover a wide frequency range with a single simulation run.

Using Maxwell's equations as starting point, this is the system of six coupled scalar equations obtained [35]:

$$\frac{\partial H_x}{\partial t} = \frac{1}{\mu}\left[\frac{\partial E_y}{\partial z} - \frac{\partial E_z}{\partial y} - (M_x + \sigma^* H_x)\right] \tag{53}$$

$$\frac{\partial H_y}{\partial t} = \frac{1}{\mu}\left[\frac{\partial E_z}{\partial x} - \frac{\partial E_x}{\partial z} - (M_y + \sigma^* H_y)\right] \tag{54}$$

$$\frac{\partial H_z}{\partial t} = \frac{1}{\mu}\left[\frac{\partial E_x}{\partial y} - \frac{\partial E_y}{\partial x} - (M_z + \sigma^* H_z)\right] \tag{55}$$

$$\frac{\partial E_x}{\partial t} = \frac{1}{\varepsilon}\left[\frac{\partial H_z}{\partial y} - \frac{\partial H_y}{\partial z} - (J_x + \sigma E_x)\right] \tag{56}$$

$$\frac{\partial E_y}{\partial t} = \frac{1}{\varepsilon}\left[\frac{\partial H_x}{\partial z} - \frac{\partial H_z}{\partial x} - (J_y + \sigma E_y)\right] \tag{57}$$

$$\frac{\partial E_z}{\partial t} = \frac{1}{\varepsilon}\left[\frac{\partial H_y}{\partial x} - \frac{\partial H_x}{\partial y} - (J_z + \sigma E_z)\right], \tag{58}$$

where $\mathbf{E}$ and $\mathbf{H}$ are the electric and the magnetic field, $\mathbf{J}$ and $\mathbf{M}$ are the electrical current density and the magnetic current density (or magnetization), ε and μ are the electrical permittivity and magnetic permeability, and σ and σ^* are the electric conductivity and the equivalent magnetic loss. This system of partial differential equations forms the basis of the FDTD numerical algorithm for electromagnetic wave interactions with general three-dimensional objects.

The Yee algorithm, which is the basis of the FDTD method, solves for both electric and magnetic fields in time t and space (x, y, z) using the coupled Maxwell's curl equations rather than solving for the electric field alone (or the magnetic field alone) with a wave equation. In order to do this, the algorithm uses a leapfrog arrangement.

All of the **E** computations in the modeled space are completed and stored in memory for a particular time point using previously stored **H** data. Then, all of the **H** computations in the space are completed and stored in memory using the **E** data just computed. The cycle begins again with the recomputation of the **E** components based on the newly obtained **H**. This process continues until time stepping is concluded. Using both **E** and **H** information, the solution is more robust than using either **E** or **H** alone. As it can be seen in Figure 19, each **E**-component is surrounded by four **H**-components, and each **H**-component is surrounded by four **E**-components.

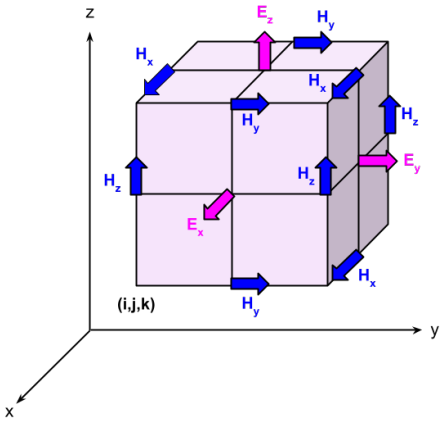

Figure 19: Position of the electric and magnetic field vector components about a cubic unit cell of the Yee space lattice.

Following this approach, we consider a uniform and rectangular lattice, where any function u of space and time, evaluated at a discrete point in the grid and at a discrete point in time, can be written as $u^n_{i,j,k} = u(i\Delta x, j\Delta y, k\Delta z, n\Delta t)$, with $\Delta x, \Delta y, \Delta z$ being the lattice space increments in the x, y, z coordinate directions, Δt is the time increment, and i, j, k, n are integers.

According to the Yee algorithm, the following equation is the first partial space derivative of u in the x direction, evaluated at the fixed time $n\Delta t$:

$$\frac{\partial u^n_{i,j,k}}{\partial x} = \frac{u^n_{i+1/2,j,k} - u^n_{i-1/2,j,k}}{\Delta x} + \Theta[(\Delta x^2)]. \tag{59}$$

The expression of the first partial space derivatives of u in the y and z directions are analogous to the previous one obtained for the x direction. The $\pm 1/2$ increment in the i subscript (x coordinate) of u denotes a space finite difference over $\pm\Delta x/2$, because the components of the electric and the magnetic field in this algorithm are interleaved in the space lattice at intervals of $\Delta x/2$.

Yee's expression for the first time partial derivative of u evaluated at the fixed space point (i, j, k) is:

$$\frac{\partial u^n_{i,j,k}}{\partial t} = \frac{u^{n+1/2}_{i,j,k} - u^{n-1/2}_{i,j,k}}{\Delta t} + \Theta[(\Delta t^2)]. \tag{60}$$

The $\pm 1/2$ increment in the n superscript (time coordinate) of u denotes a time finite difference over $\pm \Delta t/2$, so that the components of the electric and the magnetic field are interleaved in time at intervals of $\Delta t/2$ for purposes of implementing the leapfrog algorithm.

Once we define the geometry of the system and some of its properties such as conductivity, permeability and the dielectric function, and once the initial conditions are set, the values of the electric and magnetic fields can be obtained at any point of the space using both of the expressions above and the system of six differential equations.

In conclusion, the FDTD method is an extremely intuitive and easy method to solve Maxwell's equations. In fact, they can be easily solved given the initial conditions and knowing the dielectric function of the system. However, the modeled space still has to be discretized and this can lead to long computational time.

4.2. Results and discussion

We perform full electrodynamical calculations of the optical transmissivity and reflectivity of the plasmonic platform made of $Ni_{81}Fe_{19}$/Au GMR multilayers on top of a substrate of CaF_2 shown in Figure 16(a) by adopting the FDTD method implemented in the *Lumerical* software. In order to do that, we define the GMR multilayer as a material with diagonal anisotropy whose permittivity has both real and imaginary parts and is given by the dielectric tensor introduced in equation (48). We fully describe that tensor by implementing all the previously obtained data for ε_P and ε_{AP} in section 3.2.1.

The simulated structures are the following ones: an infinite GMR multilayer (Figure 20(a)) and two plasmonic plastforms with periodic structures, one of them with nanoantenna arrays made out of the GMR multilayer (Figure 20(b)), and the other one with an ordered array of holes fabricated in the GMR multilayer (Figure 20(c)).

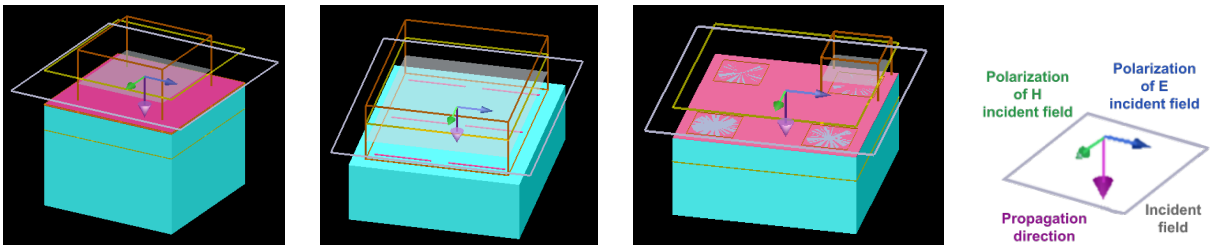

(a) (b) (c) (d)

Figure 20: $Ni_{81}Fe_{19}$/Au GMR multilayer (pink layer) on top of a CaF_2 substrate (light blue layer), simulated in the *Lumerical* software. The orange square represents the selected box in which the FDTD is applied. The yellow lines are the monitors that measure the transmissivity and reflectivity. The simulated cases are: (a) infinite multilayer, (b) arrays of nannoantennas made of the multilayer and (c) arrays of microholes in the multilayer. (d) Configuration of the source: the purple arrow represents the propagation direction of the light, and the green and blue arrow represent the polarization of the magnetic and electric field, respectively.

4.2.1 Infinite GMR multilayer

First, we consider the easiest case to simulate: an infinite GMR multilayer without any type of periodic structure added on it, such as rods, slits or holes, shown in Figure 20(a). We choose to define the material by implementing the obtained values for a multilayer of 4% GMR (Au thickness of 2.3 nm) and a multilayer of 0.8% GMR (Au thickness of 3.3 nm). Previously, we have plotted the magnetic modulation of the permitivity of both multilayers in Figure 17.

In Figure 21 we present the reflection and transmission spectra at normal incidence for the two GMR multilayer systems with different thickness of the Au layer that results in a difference of the GMR values (4% for 2.3 nm Au, 0.8% for 3.3 nm). As it can be observed, for both structures the transmissivity decreases as we increase the wavelength, with a smaller transmission as the total thickness of the structure increases. On the other hand, we observe an increase of the intensity of the reflectivity for higher wavelengths, and, within the different samples, it raises as we increase the amount of Au.

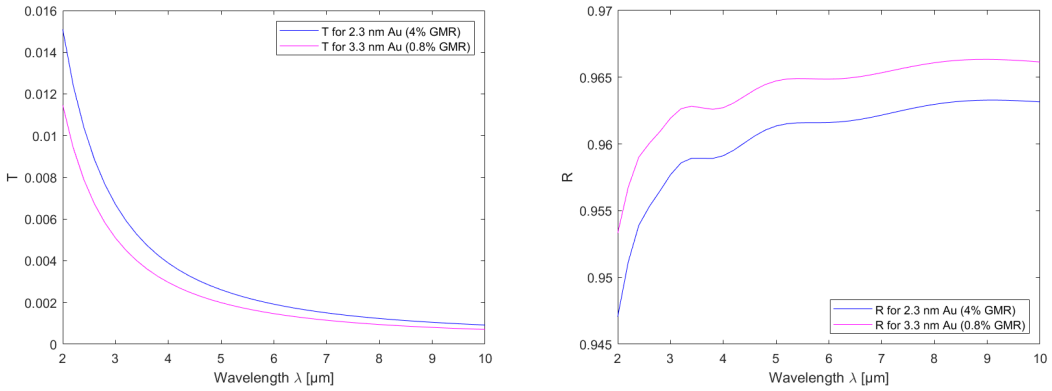

(a) (b)

Figure 21: Transmissivity (a) and reflectivity (b) at normal incidence of two infinite $Ni_{81}Fe_{19}$/Au multilayers with different Au thicknesses, and therefore different values of GMR. The pink lines represent the multilayer with 0.8% GMR (3.3 nm Au), and the blue lines represent a multilayer with 4% GMR (2.3 nm Au).

In Figure 22 we show the magnetic field modulation of the transmissivity and the reflectivity for the two multilayers with different GMR values. The curves correspond to the difference of the transmittance or reflectance between the parallel and antiparallel magnetic states of the sample and normalized to the value without magnetic field applied, as it is stated in the equation (50) for the transmission and analogously for the reflection. As it can be observed in the figure, the modulated transmission spectra $\Delta T/T$ show a broad band whose peak position and intensity depend on the GMR value. On the other hand, the magnetic modulation of the reflection shows a negative peak whose position and intensity also depend on the GMR value. Notice that, as explained in section 2.2.2, plasmons are not excited for the conditions of the simulations of the infinite GMR multilayers.

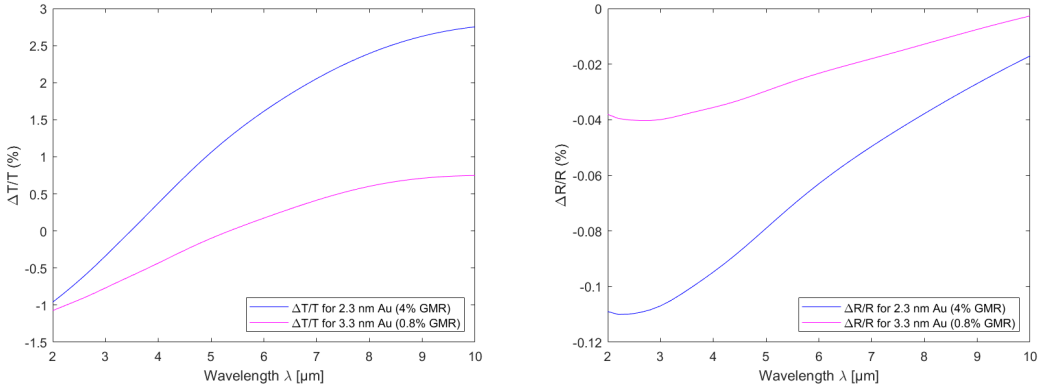

(a) (b)

Figure 22: Magnetic modulation of transmission (a) and reflection (b) spectra of light at normal incidence for two infinite $Ni_{81}Fe_{19}$/Au multilayers with different Au thicknesses, and therefore different values of GMR. The pink lines represent the multilayer with 0.8% GMR (3.3 nm Au), and the blue lines represent a multilayer with 4% GMR (2.3 nm Au).

4.2.2 Plasmonic metasurfaces: periodical structures

Based on $Ni_{81}Fe_{19}$/Au multilayers, magnetic field control of the mid IR response in a variety of metastructures has recently been demonstrated, with predicted perspectives of continuous increased modulation for longer wavelengths [4], [9], as suggested by the increasing trend of the MRE effect, i.e., $\Delta\varepsilon$ modulation, represented in Figure 17, far into the IR. Different aspects have actually been considered, such as the magnetic modulation of propagating and localized plasmons, or how the shape and size of the nanostructures affect their performance. In this section we briefly study two types of arrays added on the GMR multilayer: nanoantennas made out of the GMR multilayer (Figure 20(b)) and microholes fabricated in the GMR multilayer (Figure 20(c)).

In Figure 23(a) we represent the first simulated system, consisting of an ordered array of rectangular prism antennas [26], with antennas concentration of 2% and prism dimensions of $2 \times 0.05 \times 0.05$ μm^3 located on top of a CaF_2 substrate with refractive index $n_{CaF_2} = 1.4$ and a surface of 6×5 μm^2. The antenna material is the $Ni_{81}Fe_{19}$/Au multilayer with a GMR value of 4%. In Figure 20(b) we represent the electric field enhancement around the antenna at plasmonic resonance. In this case, localized plasmons at the antenna act as oscillating dipoles.

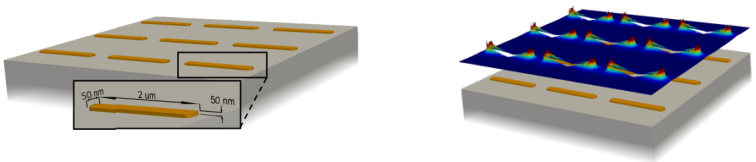

(a) (b)

Figure 23: (a) Diagram of a metamaterial platform capable of presenting localized plasmons, obtained by fabricating microantenna arrays out of multilayered continuous films. (b) Resonant excitations of the localized plasmons, susceptible to magnetic modulation via MRE control of the material's optical constants. (Both pictures obtained from [9]).

We present the calculated transmissivity at normal incidence, with the incident light polarized along the long axis of the antennas, for three multilayers with different values of spin asymmetry of the relaxation time and electron concentration. Therefore, we consider different pairs of values of α and β in the expressions (46) and (47) of ε_P and (47), respectively, of ε_{AP} that go into the dielectric tensor of equation (48). The simulated values of (α, β), all of which give a value of 4% GMR, are: (0,0.197), (-0.025,0.221) and (-0.05,0.245).

As it is shown in Figure 24(a), the transmissivity is virtually identical for the three pair of values, showing a dip around 7.5 µm that corresponds to the electric dipolar plasmonic resonance of the antenna. However, although all three structures have the same GMR value, the MRE induced changes in the optical properties are completely different. This is obvious in Figure 24(b), where the shape of the magnetic modulated transmission spectra strongly depends on the values of α and β, due to the sensitivity of the modulation of the transmissivity to the spin asymmetry of the relaxation time and electron concentration.

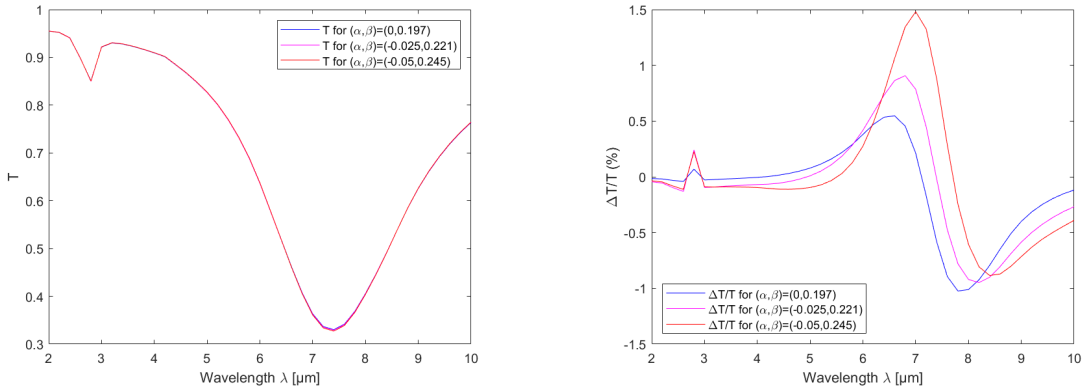

(a) (b)

Figure 24: Simulated spectra of the transmissivity (a) and its magnetic modulation (b) at normal incidence for light polarized parallel to the long axis of the antenna of an array of GMR antennas fabricated out of the $Ni_{81}Fe_{19}$/Au multilayers for different values of (α, β).

We continue the analysis of the array of nanoantennas by selecting one of the previously simulated multilayers, in this case we choose the $Ni_{81}Fe_{19}$/Au multilayer with 4% GMR whose parameters are (α, β)=(-0.05,0.245), and we perform the simulation when the incident light is polarized parallel to the long axis of the antenna prism and polarized parallel to the short axis (hence perpendicular to the long axis).

With the incident light polarized parallel to the long axis, the transmissivity shows a clear dip (continuous line in Figure 25(a)), which indicates the excitation of an electric dipolar resonance along the long rod axis. However, when the incident light is polarized along the short axis (dashed line in Figure 25(a)), no spectral features are observed in this spectral range. In Figure 25(b) we present the corresponding magnetic modulation of the transmissivity of these localized plasmon resonances, and we can clearly see that the dip-like aspect of the transmissivity of the excited mode now becomes derivative-like shape. This derivative shape is a consequence of the MRE, which produces a slight shift in the energy of the localized plasmon mode in the antenna due to the change in the refractive index of the material.

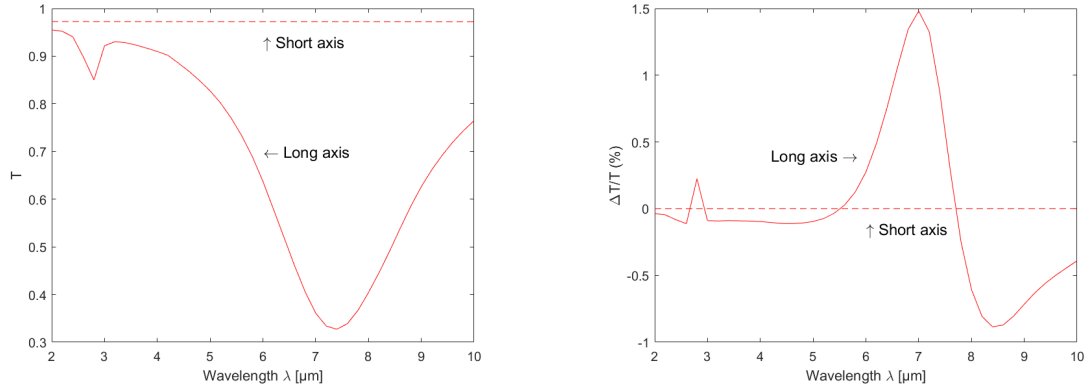

(a) (b)

Figure 25: Simulated spectra of the transmittance (a) and its magnetic modulation (b) at normal incidence of an array of GMR antennas fabricated out of the $Ni_{81}Fe_{19}$/Au multilayers for light polarized parallel (continuous line) and perpendicular (dashed line) to the long axis of the antenna prism.

To finalize the study of the antennas, we compare the transmissivity and its magnetic modulation for different lengths of the nanoantennas (1 µm, 2 µm and 3 µm), but with the same 2% concentration. Therefore, we simulate three different cases: 12 nanoantennas of length L=1 µm, 6 nanoantennas of L=2 µm and 4 nanoantennas of L=3 µm.

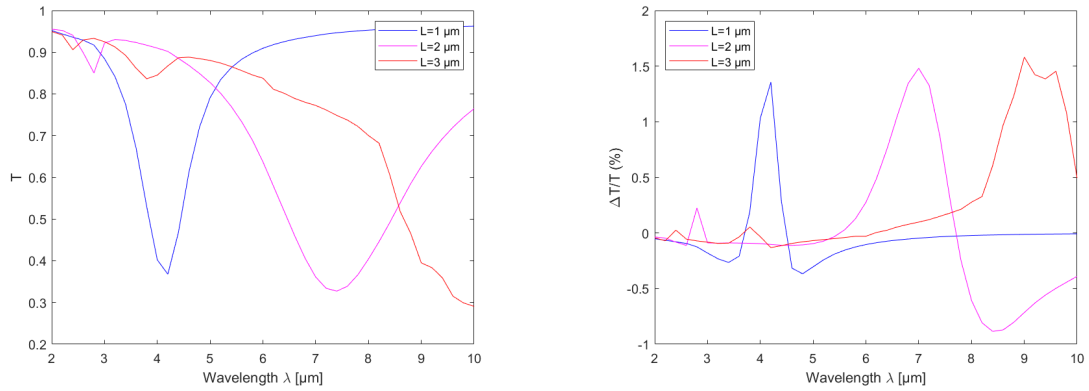

(a) (b)

Figure 26: Simulated spectra of the transmissivity (a) and its magnetic modulation (b) at normal incidence, for light polarized parallel to the long axis of the antenna prism of an array of antennas fabricated out of the $Ni_{81}Fe_{19}$/Au multilayer with 4% GMR for three different rod lengths: L=1 µm (pink line), L=2 µm (red line) and L=3 µm (blue line).

In Figure 26(a) we can clearly observe in the transmission spectrum the profound dips that correspond to the the excitation of the plasmon resonances localized at the rods. As we increase the length of the antenna, the position of the resonances shift towards longer wavelengths, red-shifts, and the dip is more pronounced. In Figure 26(b) we represent the magnetic modulation of the transmission for the same rod arrays. These spectra also show a derivative like features at the position of the rod resonances, mentioned above.

The last plasmonic-spintronic metasurface studied in this work is an ordered array of circular holes of radius R=1 µm fabricated in the $Ni_{81}Fe_{19}$/Au multilayer located on top of the CaF_2 substrate [9], shown in Figure 27(a). The simulation conditions are depicted in Figure 20(c).

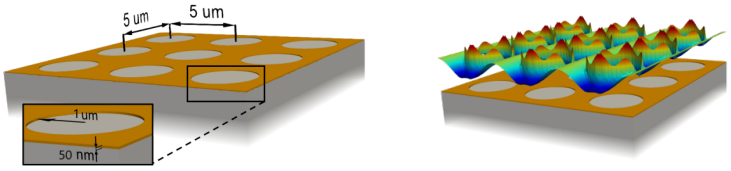

(a) (b)

Figure 27: (a) Diagram of a metamaterial platform capable of presenting propagating plasmons, obtained by fabricating hole arrays out of multilayered continuous films. (b) Electric field enhancement around the holes due to the propagating plasmons, susceptible to magnetic modulation via MRE control of the material's optical constants. (Both pictures obtained from [9]).

We consider two different samples of the multilayer, both of the hole arrays patterned with a 5 µm periodicity. Both samples have different Au thicknesses, and hence different values of GMR: The first sample is the multilayer with 4% GMR (2.3 nm Au thickness), and the other sample has 0.8% GMR (3.3 nm Au thickness). Both multilayers are the same ones we simulated in the case of the infinite GMR multilayers.

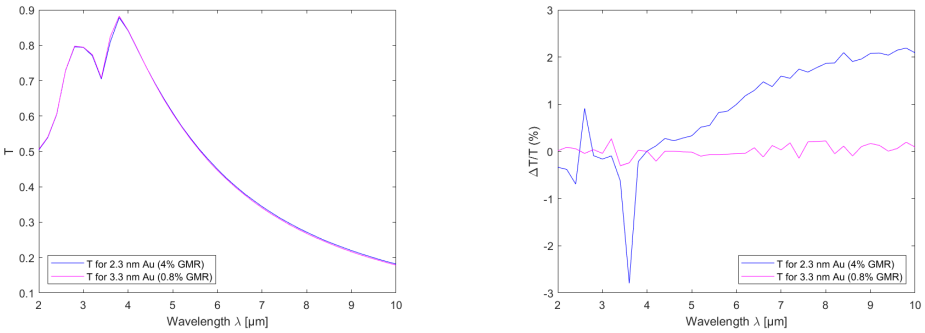

(a) (b)

Figure 28: Simulated spectra of the transmissivity (a) and its magnetic modulation (b), at normal incidence for an ordered array of circular micrometric holes fabricated on $Ni_{81}Fe_{19}$/Au multilayers with 4% GMR (blue lines) or with 0.8% GMR (pink lines).

In Figure 28(a) we present transmission spectra for these two samples, with well-defined peaks known to be associated to the excitation of propagating plasmons (SPPs) at the air-multilayer and multilayer-substrate interfaces. As both samples have the same periodicity (and just an slightly different amount of Au thickness) the transmission spectra is basically the same for both of them. In Figure 28(b) we show the magnetic field modulation of the transmission for both structures. In the multilayer with 4% GMR, again derivative-like features are observed in the spectral positions corresponding to the resonances. However, no feature whatsoever is observed in the multilayer with barely any GMR (0.8% GMR). For that reason, it can clearly be concluded that the GMR is the underlying mechanism behind this magnetic modulation, specifically the MRE that changes the optical constants of the GMR multilayer due to this spintronic effect.

5. Conclusions

In the present work, we have studied how Spintronics and Photonics interact in the common space offered by the Magneto-refractive effect (MRE), making it possible to develop active photonic systems utilizing spintronic mechanisms. We have first introduced some main concepts of Plasmonics, such as Localized Surface Plasmons (LSPs) and Surface Plasmon Polaritons (SPPs), but we have focused on the last ones. After giving a proper definition of SPPs and discussing some of the fundamental optical properties of metals, we have defined and graphically represented their dispersion relation at a single interface, as well as indicated different experimental arrangements to excite them.

Then, we have explained the main spintronic phenomenon capable of efficiently affecting the optical properties of different photonic platforms: the Giant Magnetoresistance (GMR). Due to this effect, when a magnetic field is applied to a GMR multilayer, the magnetizations of the ferromagnetic layers go from being antialigned with respect to the adjacent layers to being aligned, leading to changes in the electrical conductivity.

We have followed the explanation of the GMR with an analysis of the MRE properties in the GMR multilayers. First, we have defined the conductivity σ, and the related permittivity ε, for both parallel and antiparallel orientations of the ferromagnetic layers. Since the permittivity is directly related to the complex refractive index, that variation in conductivity also generates a variation in the optical properties of the system, such as the transmission and the reflection. Therefore, when there is no magnetic field applied, the effective dielectric response of the system is given just by the permittivity in the antiparallel configuration, ε_{AP}. However, when there is an applied magnetic field, the dielectric constant that defines the system is given by a tensor whose diagonal components are ε_P, ε_P and ε_{AP}.

We have studied the case of a $Ni_{81}Fe_{19}$/Au GMR multilayer on a CaF_2 substrate and analysed some of its optical properties for different cases. We have represented the effective dielectric constant (ε_{AP}), the magnetic modulation of the dielectric constant ($\Delta\varepsilon = \varepsilon_P - \varepsilon_{AP}$), the transmissivity T, the reflectivity R and the magnetic modulation of both properties ($\Delta T/T$ and $\Delta R/R$) for different values of Au thicknesses (and therefore different values of the GMR). From those simulations, we have concluded that, despite the fact that the effective dielectric constants are very similar for the different GMR values of the multilayer, the intensity of the magnetic modulation of those constants increases as we increase the GMR value. Furthermore, the transmissivity increases as the GMR value is increased, whereas the reflectance decreases. Analogously, the modulated T and R show a peak position and intensity that completely depends on the GMR value. For the sample with a higher GMR value, the peak of the transmissivity is higher, hence lower in the reflectivity.

Moreover, we have shown that the magnetic modulation of the dielectric constant depends strongly on the values of α and β, which are parameters that appear in the equations that define ε_P and ε_{AP} and reflect the spin asymmetry in the electron concentration and in the relaxation times, respectively.

Finally, we have presented some of the current approaches to achieve active photonic platforms. We have studied two different types of spintronic-plasmonic metasurfaces: an array of nanoantennas made out of the GMR multilayer and an ordered array of microholes fabricated in the GMR multilayer. For the case of the nanoantennas, we have simulated the array for different cases, with the purpose of comparing the transmissivity T and its magnetic modulation $\Delta T/T$ when some properties of the system, such as the length of the antennas, change. Firstly, after comparing T and $\Delta T/T$ for different values of (α, β) we have learnt that the magnetic modulation of the transmissivity relies totally on the spin asymmetry of the relaxation time and electron concentration. Then, we have obtained $\Delta T/T$ when the incident light is parallel to the long axis of the prism antenna and parallel to the short axis (i.e. perpendicular to the long axis), and we have compared both cases, concluding that the excitation of the electric dipolar resonances can only be observed when the incident light is parallel to the long axis. Finally, we have studied T and its magnetic modulation again but for different lengths of the antennas, and we have clearly observed that the position of the plasmons' resonance shifts towards longer wavelengths.

For the case of the microholes, we have simulated the array for two different thicknesses of Au, and therefore two different values of the GMR: one of the multilayers with an Au thickness of 2.3 nm, hence 4% GMR, and the other one with an Au thickness of 3.3 nm, hence 0.8% GMR. From those representations, we have proved that the GMR is the main responsible effect for the magnetic modulation of the optical properties. All the mentioned simulations have been done with the photonic simulation software *Lumerical*, that applies the Finite-difference time-domain (FDTD) method to predict how light behaves within complex structures.

Regardless of all the particular conclusions obtained throughout this work, there is still much research that needs to be done about the overlap between Spintronics and Photonics, such as exploring spintronic platforms capable of exhibiting large MRE values while maintaining low working magnetic fields. For this improvement of the performance of MRE based photonic platforms, it would be necessary to study the huge diversity of spintronic materials, not only GMR multilayers, and to examine the use of metamaterials to maximize the electromagnetic field at the position of the spintronic component. The next step to test the sensing abilities of the studied metasurfaces would be to cover them with molecules, with a characteristic refractive index and study the variations in the magnetic field modulation of the optical properties, following reference [10].

References

[1] H.-T. Chen, A. J. Taylor, and N. Yu, "A review of metasurfaces: physics and applications," *Reports on Progress in Physics*, vol. 79, no. 7, p. 076401, jun 2016.

[2] N. Yu and F. Capasso, "Flat optics with designer metasurfaces." *Nature materials*, vol. 13, pp. 139–50, 2014.

[3] S. M. Choudhury, D. Wang, K. Chaudhuri, C. DeVault, A. V. Kildishev, A. Boltasseva, and V. M. Shalaev, *Nanophotonics*, vol. 7, no. 6, pp. 959–987, 2018.

[4] G. Armelles, L. Bergamini, N. Zabala, M. U. González, F. García, R. Alvaro, J. Aizpurua, and A. Cebollada, "Broad band infrared modulation using spintronic-plasmonic metasurfaces," *Nanophotonics*, vol. 8, no. 10, pp. 1847–1854, 2019. [Online]. Available: https://doi.org/10.1515/nanoph-2019-0183

[5] G. Armelles, L. Bergamini, A. Cebollada, M. U. González, R. Álvaro, L. Torné, N. Zabala, and J. Aizpurua, "Magnetic modulation of far- and near-field ir properties in rod-slit complementary spintronic metasurfaces," *Opt. Express*, vol. 28, no. 22, pp. 32 584–32 600, Oct 2020. [Online]. Available: https://opg.optica.org/oe/abstract.cfm?URI=oe-28-22-32584

[6] G. Binasch, P. Grünberg, F. Saurenbach, and W. Zinn, "Enhanced magnetoresistance in layered magnetic structures with antiferromagnetic interlayer exchange," *Phys. Rev. B*, vol. 39, pp. 4828–4830, 1989.

[7] M. N. Baibich, J. M. Broto, A. Fert, F. N. Van Dau, F. Petroff, P. Etienne, G. Creuzet, A. Friederich, and J. Chazelas, "Giant magnetoresistance of (001)fe/(001)cr magnetic superlattices," *Phys. Rev. Lett.*, vol. 61, pp. 2472–2475, 1988.

[8] J. C. Jacquet and T. Valet, "A new magnetooptical effect discovered on magnetic multilayers: The magnetorefractive effect," *MRS Online Proceedings Library (OPL)*, vol. 384, p. 477, 1995.

[9] G. A. Reig, L. Bergamini, N. Zabala, F. García-Pérez, M. L. Dotor, L. Torné, R. Álvaro Bruna, A. Griol, A. Martínez, J. Aizpurua, and A. Cebollada, "Metamaterial platforms for spintronic modulation of mid-infrared response under very weak magnetic field," *ACS Photonics*, vol. 5, no. 10, pp. 3956–3961, 2018.

[10] G. Armelles, L. Bergamini, A. Cebollada, N. Zabala, and J. Aizpurua, "A novel vibrational spectroscopy using spintronic–plasmonic antennas: Magneto-refractive surface-enhanced infrared absorption," *Journal of Applied Physics*, vol. 129, no. 7, 02 2021.

[11] R. F. Aroca, D. J. Ross, and C. Domingo, "Surface-enhanced infrared spectroscopy," *Applied Spectroscopy*, vol. 58, no. 11, pp. 324A–338A, 2004.

[12] H.-L. Wang, E.-M. You, R. Panneerselvam, S.-Y. Ding, and Z.-Q. Tian, "Advances of surface-enhanced raman and ir spectroscopies: from nano/microstructures to macro optical design," *Light: Science Applications*, vol. 10, no. 1, p. 161, 2021.

[13] F. Neubrech, C. Huck, K. Weber, A. Pucci, and H. Giessen, "Surface-enhanced infrared spectroscopy using resonant nanoantennas," *Chemical reviews*, vol. 117, no. 7, pp. 5110–5145, 2017.

[14] W. Lin and M. Sun, *Noble Metal-Metal Oxide Hybrid Nanoparticles*, ser. Micro and Nano Technologies. Woodhead Publishing, 2019.

[15] S. Maier, *Plasmonics: Fundamentals and Applications*, 01 2007.

[16] J. Zhang, L. Zhang, and W. Xu, "Surface plasmon polaritons: physics and applications," *Journal of Physics D: Applied Physics*, vol. 45, no. 11, p. 113001, feb 2012. [Online]. Available: https://dx.doi.org/10.1088/0022-3727/45/11/113001

[17] L. Novotny and B. Hecht, *Principles of Nano-Optics*, 2nd ed. Cambridge University Press, 2012.

[18] A. Otto, "Excitation of nonradiative surface plasma waves in silver by the method of frustrated total reflection," *Zeitschrift für Physik A Hadrons and nuclei*, vol. 216, pp. 398–410, 1968.

[19] E. Kretschmann, "Die bestimmung optischer konstanten von metallen durch anregung von oberflächenplasmaschwingungen (the determination of the optical constants of metals by excitation of surface plasmons)," *Zeitschrift für Physik A Hadrons and nuclei*, vol. 241, pp. 313–324, 1971.

[20] C. Simovski and S. Tretyakov, *An Introduction to Metamaterials and Nanophotonics*. Cambridge University Press, 2020.

[21] R. Weiss, R. Mattheis, and G. Reiss, "Advanced giant magnetoresistance technology for measurement applications," *Measurement Science and Technology*, vol. 24, p. 082001, 07 2013.

[22] G. Armelles and A. Cebollada, "Active photonic platforms for the mid-infrared to the thz regime using spintronic structures," *Nanophotonics*, vol. 9, no. 9, pp. 2709–2729, 2020. [Online]. Available: https://doi.org/10.1515/nanoph-2020-0250

[23] K. Wu, D. Tonini, S. Liang, R. Saha, V. K. Chugh, and J.-P. Wang, "Giant magnetoresistance biosensors in biomedical applications," *ACS applied materials interfaces*, vol. 14, no. 8, pp. 9945–9969, 2022. [Online]. Available: https://doi.org/10.1021/acsami.1c20141

[24] T. Haider, "A review of magneto-optic effects and its application," *International Journal of Electromagnetics and Applications*, vol. 7, no. 1, pp. 17–24, 2017.

[25] M. Faraday, "Experimental researches in electricity. nineteenth series," *Philosophical Transactions of the Royal Society of London*, vol. 136, pp. 1–20, 1846. [Online]. Available: http://www.jstor.org/stable/108303

[26] G. Armelles, A. Cebollada, and F. García, "Au dependence of the mid infrared optical and magnetorefractive properties of ni81fe19/au gmr multilayers," *Opt. Mater. Express*, vol. 9, no. 2, pp. 923–931, Feb 2019. [Online]. Available: https://opg.optica.org/ome/abstract.cfm?URI=ome-9-2-923

[27] J. van Driel, F. R. de Boer, R. Coehoorn, G. H. Rietjens, and E. S. J. Heuvelmans-Wijdenes, "Magnetorefractive and magnetic-linear-dichroism effect in exchange-biased spin valves," *Phys. Rev. B*, vol. 61, pp. 15 321–15 326, Jun 2000. [Online]. Available: https://link.aps.org/doi/10.1103/PhysRevB.61.15321

[28] M. Born and E. Wolf, *Principles of Optics: Electromagnetic Theory of Propagation, Interference and Diffraction of Light*, 7th ed. Cambridge University Press, 1999.

[29] J. R. Reitz, F. J. Milford, and R. W. Christy, *Foundations of Electromagnetic Theory (4th Edition)*, 4th ed. Addison-Wesley Publishing Company, 2008.

[30] J. A. Stratton, *Electromagnetic Theory*. McGraw Hill, 1941.

[31] M. Vopsaroiu, T. Stanton, O. Thomas, M. Cain, and S. M. Thompson, "Infrared metrology for spintronic materials and devices," *Measurement Science and Technology*, vol. 20, no. 4, p. 045109, mar 2009. [Online]. Available: https://dx.doi.org/10.1088/0957-0233/20/4/045109

[32] "Ansys lumerical." [Online]. Available: https://www.lumerical.com/

[33] M. N. O. Sadiku, *Numerical Techniques in Electromagnetics with MATLAB*. CRC Press, 2009.

[34] K. Yee, "Numerical solution of initial boundary value problems involving maxwell's equations in isotropic media," *IEEE Transactions on Antennas and Propagation*, vol. 14, no. 3, pp. 302–307, 1966.

[35] A. Taflove and S. Hagness, *Computational Electrodynamics: The Finite-Difference Time-Domain Method, 3rd edition.*, 06 2005, vol. 2062.